POLITECNICO DI TORINO

Master’s Degree in Energy and Nuclear Engineering

CFD MODELLING FOR THE CHARACTERIZATION OF FAST-PYROLYSIS BIO-OIL (FPBO) ATOMIZATION

Supervisors	**Candidate**
Prof. Mirko Baratta	Stefania Siragusa
Prof.ssa Daniela Anna Misul	
Prof. Simone Salvadori	
Dott. Ing. Prashant Goel	

A.Y. 2020/2021

N

Index

Abstract

Fast pyrolysis bio-oil (FPBO) is considered a good substitute for conventional fuel oils in several application, such as boilers, furnaces, and gas turbines. This bio-oil has different physical and chemical properties compared to the one of petroleum and other bio-oils. In fact, as it has been widely demonstrated in many studies, this replacing needs some modifications of the already existing technology to be adapted to work with FPBO.

The aim of this thesis is to investigate how to set up a CFD model of a nozzle with FPBO, and to analyse the average size of the spray particles for future applications in gas turbines. To achieve this purpose an initial literature review has been done to have an overview on the studies already done about FPBO and its characteristics. Particular attention was paid to works focused on the evolution of spray performance of FPBO. Most of them showed that, due to the uncommon properties of FPBO, the atomization of this fuel with pressure atomizers is not so efficient, but different results have been achieved with twin-fluid nozzles. For this reason, as starting point for the creation of a CFD model was chosen the experimental work of Sangsig Yun et al., who obtained, using an air blast nozzle, a FPBO spray with Sauter mean diameter (SMD) of 50 microns.

For the setting up of the CFD model, it has been necessary to select a surrogate and to define its physical and chemical properties. In parallel a 3D model has been developed in order to simplify the original nozzle used in the experimental work.

The CFD model has been created thanks to the innovative software CONVERGE, the strength of this software is the capability to create an autonomous mesh, reducing in this way the total computational time. Once the CFD model was ready the results have been post-processed by Tecplot, another common software. Finally, to validate the results performed by the simulation, they have been compared with the one obtained in the experimental work of Sangsig Yun et al., showing a good similarity.

KEYWORDS: CFD, FPBO, Atomization

1. **Introduction**

An important challenge of nowadays is to reduce the greenhouse gas emissions, which are largely produced by combustion systems. Nevertheless, the dependence on combustion, as an energy source, is unlikely to decrease in the near future. So, it is worth to find solutions to make fuel sources themselves more environmentally friendly.

Fast pyrolysis bio-oil (FPBO), a liquid fuel created from biomass, is considered the most promising substitute in the replacement of petroleum-derived liquid fuels. In fact, it is the lowest cost liquid biofuel available. In addition, it is a second-generation biofuel, that means that it is made from non-edible biomass feedstocks, and so it does not compete for agricultural space or with food delivery. FPBO can be made from several variety of biomass feedstocks, but these are commonly lignocellulosic materials generated by waste wood. Therefore, it has a good potential to be used in commercial applications such as burners, boilers, furnaces, gas turbine and compressions-ignition engines.

Anyway, the combustion characteristics of any liquid fuel are strongly dependent on the quality of the fuel atomization. As already known, an efficient spray combustion needs a proper vaporization of the fuel and a good mixing between fuel and oxidizer. As well as it needs an ignition and completely burning within the residential time and the volume of the combustor. To satisfy these requirements, a fine-droplet spray with a uniform distribution is necessary.

FPBO is a promising and inexpensive alternative to fossil oils, but its application is at the same time a challenge. In fact, due to its very different chemical and physical properties with respect to conventional fuels, the already existing technology needs to be adapted. As consequence of that, a detailed study about the atomization of FPBO is fundamental, not for nothing, in the last decades, a lot of effort in this direction has been spent (and is going to be) by researchers.

An accurate investigation of FPBO atomization requires both numerical and experimental research. Since, experiments are expensive and time consuming, a combination with a Computational Fluid Dynamics (CFD) analysis can make the difference. In fact, if a CFD model is well settled can supply an accurate simulation of the reality, thus allowing to save time and money.

To conclude, the main purpose of this thesis is to develop a CFD model, which can simulate the atomization of FPBO. After a literature review, the developing of the model has been permed thanks to the software called CONVERGE, that supplies an efficient method to simulate sprays, combining Eulerian and Lagrangian models.

1.1 Outline

This thesis work is divided into eleven chapter:

- The first chapter is the introduction, where the main topic of thesis is introduced to the reader.
- In the second one the main concepts about atomization and spray are discussed, especially the concepts which have been useful for the scope of this thesis.
- In the third one the most relevant characteristics of FPBO are summarised. The advantages and disadvantages have been reported, as well as the current and potential application.
- In the fourth one, the main characteristics, which have been investigated by experimental works, are reported.
- In the fifth chapter some basic knowledges about what CFD analysis is, how a turbulent problem is faced, and which are the main models, especially RANS one, have been introduced.
- In the sixth one the innovative software CONVERGE has been presented, especially the main tools, supplied by the software and fundamental for the development of this project, such as the mesh refinement tools and the VOF-Spray One-Way Coupling.
- In the seventh chapter, it has been the summarised the experimental work of S.Yun. This work has been selected as reference model for the development of a numerical model, capable to reproduce the atomization of FPBO.

- In the nineth chapter, the already available FPBO surrogate, supplied by A.Frassoldati, has been discussed. Moreover, it has been adapted to the physical properties of the sample used in the tests performance by S.Yun.
- In the tenth one, it has been explained how the numerical model has been developed, starting from the creation of the 3D model to the setup of the simulations.
- In the eleventh one, the results obtained are reported and discussed.
- Finally, in the last chapter, an overview of the work done, and some future proposals are present.

2. **Atomization and Sprays**

The atomization of a bulk liquid into droplets ranging in size from submicron to some hundred microns in diameter is required in several industrial processes such us spray combustion, evaporative cooling, drop spraying, spray drying and other applications in the fields of medicine, printing, and meteorology. With this purpose many devices have been developed such us atomizers, sprayers, and nozzles.

It is called spray a system of droplets immersed in a gaseous continuous phase. To obtain this effect there are more than one way, the most common devices achieve atomization by producing a high velocity between the liquid and the surrounding gas, generally air.

Pressure, rotary, or twin-fluid type atomizers are very popular. However, there are also other less popular types that are useful in special applications, electrostatic and ultrasonic devices are two of them. For the electrostatic one the atomization driving force is intense electrical pressure, in the ultrasonic one the liquid to be atomized is fed through or over a transducer which vibrates at ultrasonic frequencies to produce the short wavelengths required to produce small droplets. Both atomizers can achieve fine atomization, but they can atomize only low liquid flow rates and for this reason their applicability is limited.

2.1 Basic Processes

Each spray is characterized by a shape, a structure, and a penetration length, as well as a droplet velocity and a drop size distribution. All these characteristics are strongly affected by the basic process associated, that depends on the atomizer size and geometry, the physical properties of the liquid, and the properties of the gaseous medium into which the liquid stream is discharged. The liquid properties most involved in the atomization are the surface tension, the viscosity, and the density.

Generally, atomization can be considered as a disruption of the consolidating influence of surface tension by the action of internal and external forces. In the absence of such disruptive forces, surface tension tends to pull the liquid into the form of a sphere, since this has the minimum surface energy. Liquid viscosity exerts a stabilizing influence by opposing any change in system geometry. On the other hand, aerodynamic forces acting on the liquid surface may promote the disruption process by applying an external distorting force to the bulk liquid. Breakup occurs when the magnitude of the disruptive force just exceeds the consolidating surface tension force [2].

In most cases, to atomization is affected also by turbulence in the liquid, cavitation in the nozzle, and aerodynamic interaction.

Many of the larger drops produced in the initial disintegration process are unstable and undergo further disruption into smaller drops. Thus, the final range of drop sizes produced in a spray depends not only on the drop sizes produced in primary atomization, but also on the extent to which these drops are further disintegrated during secondary atomization [2].

2.2 Breakup of Drops

Basically, the atomization of a liquid surrounded by air involves many interacting mechanisms, one of these is the splitting up of the larger drops during the final stages of disintegration, due to the action of aerodynamic forces.

To solve the breakup of a drop in a rigorous mathematical way, the exact distribution of the aerodynamic pressure on the drop is required. However, every time the drop is deformed also the pressure distribution changes.

Under equilibrium conditions, p_I, the internal pressure at any point on the drop surface, balances p_A the external aerodynamic pressure, and p_σ, the surface tension pressure[2]:

$$p_I = p_A + p_\sigma \tag{1}$$

Where p_σ, for a spherical drop with a diameter D, is:

$$p_\sigma = \frac{4\sigma}{D} \tag{2}$$

The drop is stable until the change in p_A are small enough to be compensated by a corresponding change in p_σ. But, when the external pressure, p_A, is too large to be compensated by p_σ, the internal pressure, p_I, is not constant anymore and p_A can deform the drop to an extent that leads to further reduction in p_σ and finally to disruption of the drop into smaller drops. This subdivision may occur again, with the new smaller drops, until when p_σ is large enough to compensate p_A. When this stage is reached, the drop is stable, and no further breakup can occur.

Note that decreasing the droplet diameter, the breakup time will increase accordingly until the stable drop size for which an infinite breakup time is attained.

Considering a droplet breakup in flowing air, many theories have been formulated since the twentieth century. The flow pattern around the liquid droplets affects how the aerodynamic forces act on them and deform them. Three types of deformation were identified by J. O. Hinze [3] (see **Figure 1**):

1. *Lenticular deformation:* The drop is flattened to form an oblate ellipsoid. Subsequent deformation depends on the magnitude of the internal forces causing the deformation.
2. *Cigar-shaped deformation:* The initial drop becomes elongated to form a long cylindrical thread or ligament that breaks up into small drops.
3. *Bulgy deformation:* Local deformations on the drop surface create bulges and protuberances that eventually detach themselves from the parent drop to form smaller drops.

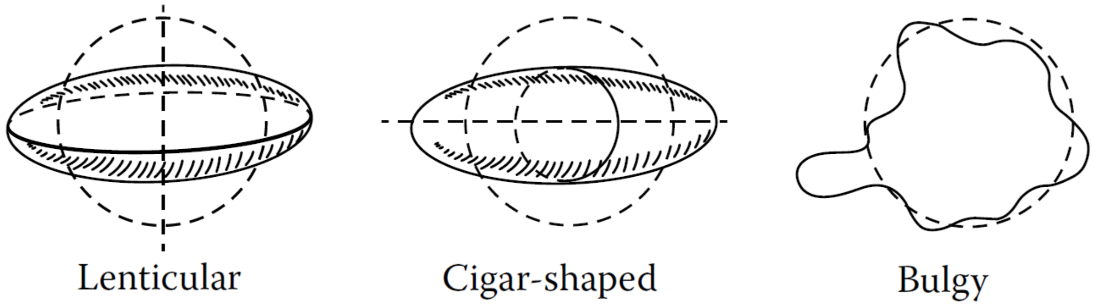

Figure 1 *Basic types of globule deformation (Lenticular type on the left, Cigar-shaped type at the centre and Bulgy type on the right).*

The preference for any particular type of deformation depends partly on the physical properties of the gas and liquid phases (densities, viscosities, and interfacial tension), and on the flow pattern around the drop.

2.3 Breakup of Liquid Jets

When a liquid jet comes out from a nozzle as a continuous body of cylindrical form, the imbalance on the surface of the jet between the cohesive and disruptive forces leads to oscillations and perturbations. Under favorable conditions, the primary atomization takes place, the oscillations are amplified, and the liquid body disintegrates into drops. If the drops so formed exceed the critical size, they continue to disintegrate into smaller drops, a process known as secondary atomization [2].

The jet disintegration is a complex phenomenon under study since a long time. A relevant contribution has been supplied by Rayleigh, in an early mathematical analysis, he used the method of small disturbances to predict the conditions necessary to cause the collapse of a liquid jet issuing at low velocity, for example, a low-speed water jet in air. Comparing the surface energy of the disturbed configuration to that of the undisturbed column, the following equation can be written:

$$E_s = \frac{\pi\sigma}{2d}(\gamma^2 + n^2 - 1)b_n^2 \tag{3}$$

Where E_s is the potential surface energy, d the jet diameter, b_n a constant in the Fourier series expansion, γ the dimensionless wave number ($\frac{2\pi}{\lambda}$), λ the wavelength of disturbance and n any positive integer.

When E_s is positive means that the system is stable to those classes of disturbance, but when it is negative the system is unstable.

Rayleigh's conclusion, on the breakup of a no viscous liquid jets under laminar flow conditions, were that all disturbances on a jet with wavelengths greater than its circumference will grow. Moreover, his results show that one class of disturbance will grow fastest and eventually control the breakup.

The conclusions of Rayleigh have found general acceptance in later theories as valid first approximations, although real liquid jets are viscous, turbulent, and subjected to surrounding air influences.

Rayleigh demonstrated that for this preliminary study the average drop size is nearly twice the diameter of the undisturbed jet.

In fact, by assuming that b_n from the Equation (3) is proportional to $\exp(qt)$, q is the exponential growth rate of disturbance, the exponential growth rate of the fastest-growing disturbance is given by:

$$q_{max} = 0.97\left(\frac{\sigma}{\rho_L d^3}\right)^{0.5} \tag{4}$$

And λ_{opt}, corresponding to q_{max}, is:

$$\lambda_{opt} = 4.51d \tag{5}$$

So, after the breakup, the cylinder of length λ_{pot} becomes a spherical drop, so that:

$$4.51d\frac{\pi}{4}d^2 = \frac{\pi}{6}D^3 \tag{6}$$

And the diameter D of the drop is:

$$D = 1.89d \tag{6}$$

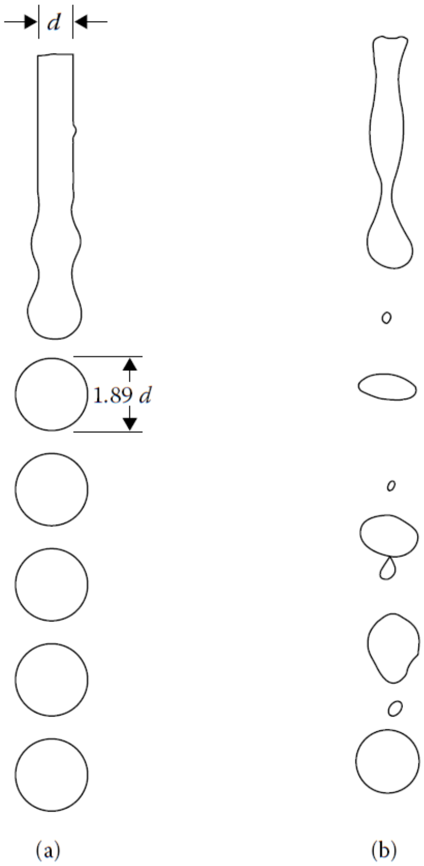

Figure 2 *Comparison of idealized jet (a) breakup with actual (b) breakup.*

As shown in the **Figure 2(a)** the ideal jet is quite regular and the drops, which are generated, are of uniform size and spacing. But in the reality the jets are different, in **Figure 2(b)** an actual jet breakup, based on high-speed photographs, is reported and the formation and growth of axisymmetric disturbances are evident [4][2].

In 1931, Weber extended Rayleigh's work, which considers the surface tension and inertial forces but neglects viscosity and the effect of the surrounding air, to also include the effect of air resistance on the disintegration of a jet into drops. Weber showed that air friction reduces the optimum wavelength for the drop formation. For example, with a zero-relative velocity, he found that λ_{opt} is $4.44d$, quite close to the value predicted by Rayleigh ($4.51d$) at same conditions, and with a relative velocity of $15\,\frac{m}{s}$ he showed that λ_{opt} is $2.8d$ and that the drop diameter is $1.6d$. In different words, higher is the relative velocity between the liquid jet and the surrounding air smaller is the λ_{opt} for the breakup and so also the drop size.

After that Weber also examined the effect of liquid viscosity on the jet disintegration, finding that higher is the viscosity of liquid larger is the λ_{opt} for the jet breakup:

$$\lambda_{opt} = 4.44d\ (1 + 3\ Oh)^{0.5} \tag{6}$$

Where the Ohnesorge number (Oh) is defined as:

$$Oh = \frac{\mu_L}{(\rho_L \sigma d_o)^{0.5}} \tag{7}$$

Another relevant contribution to this topic has been supplied by Haenlein, he observed four different regimes of breakup in the disintegration of a liquid jet

1. *Drop formation without the help of air.* This is the same mechanism studied by Rayleigh, it is characterized by linear relationship between the jet velocity and the length of the jet. Weber showed that in this case the breakup time is proportional to $d_o^{1.5}$, where d_o is the orifice nozzle diameter, for no viscous fluids and proportional to d_o for viscous jets (see **Figure 3**(a)).
2. *Drop formation with air influence*. As the jet velocity increases, the aerodynamic forces of the surrounding air are more relevant, and the waves formed more accentuate (see **Figure 3**(b)).
3. *Drop formation due to waviness of the jet*. In this case the effectiveness of the aerodynamic forces is increasing, and the influence of the surface tension is decreasing (see **Figure 3**(c)).
4. *Drop formation at the nozzle in a chaotic and irregular manner*.

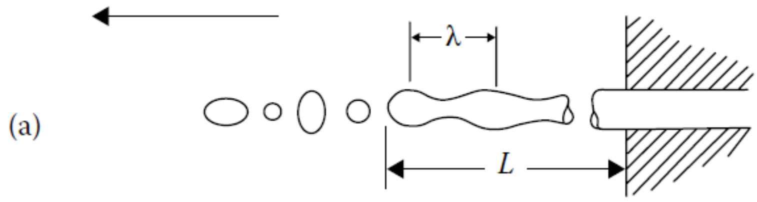

Oscillations cause jet breakup. No air friction.

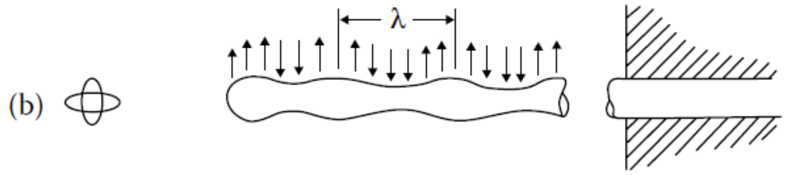

Oscillations with air friction.

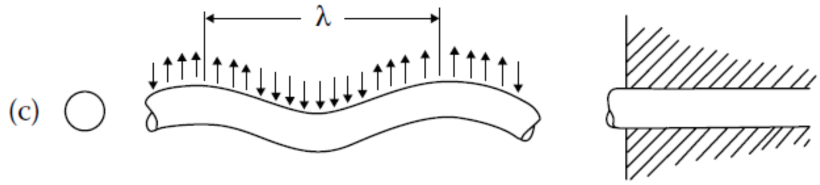

Wave-like breakup caused by air friction.

Figure 3 *Mechanisms of drop formation.*

Another common criterion for classifying jet disintegration is the one proposed by Ohnesorge, he used a dimensionless analysis to describe the disintegration of a jet in three stages, each stage is characterized by Reynolds number, Re, and the Ohnesorge number, Oh.

As reported in the **Figure 4** the breakup mechanisms of jets can be divided into three regions on a graph of Oh versus Re:

1. In the first region (I), at low Re, the jet breaks up into large drops of quite uniform size, this is the Rayleigh mechanism of disintegrations.
2. In the second region (II), the breakup of the jet is due to the oscillations with respect to the jet axis, the intensity of these oscillations increases until the jet disintegrates into drops with a wide range of sizes.
3. In the third region (III), at high Re, the atomization is complete close to the discharge orifice.

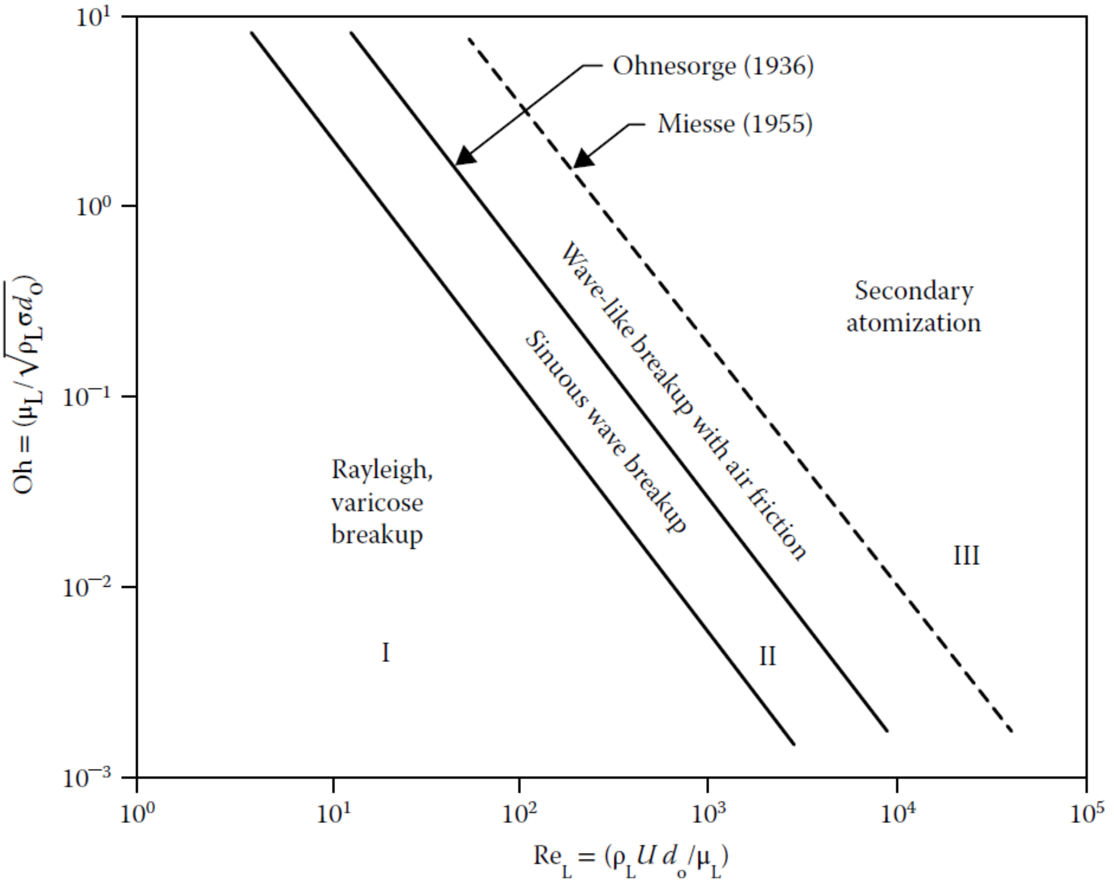

Figure 4 *Classification of modes of disintegration of a jet by Ohnesorge.*

2.4 Drop Size Distribution

Common atomizers produce droplets in a wide range of drop sizes, ranging from few microns up to several hundred microns. An easy way to visualize the droplet size distribution is to plot a histogram where each ordinate represents the number of droplets whose size is included into the limits $D - \frac{\Delta D}{2}$ and $D + \frac{\Delta D}{2}$. As consequence, the smaller is ΔD the more the histogram resemble to a frequency distribution curve.

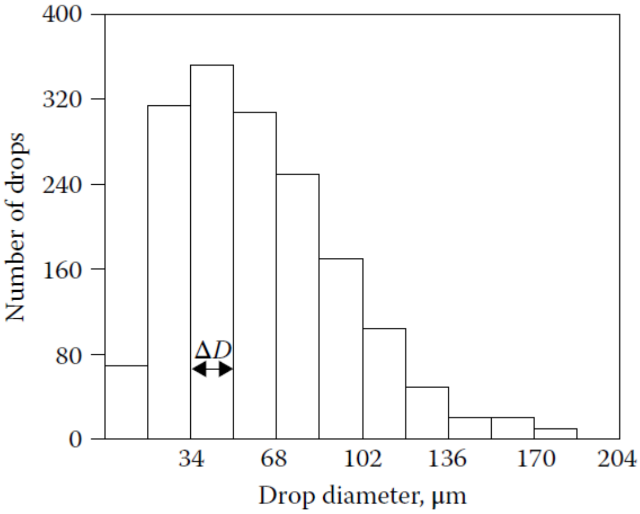

Figure 5 *Example of a spectrum of drop sizes.*

The graphical representation of drop size distribution can be elaborate, so several attempts to simplify this process with mathematical expressions have been made.

Suitable mathematical expressions would satisfy the following requisites:

- Provide a satisfactory fit to the drop size data.
- Allow extrapolation of drop measurements even if out of the range of measured values.
- Allow an easy calculation of the average and representative drop diameters and other relevant parameters.
- Permit to elaborate a large amount of data.
- Ideally, provide some information into the basic mechanisms involved in atomization.

The most widely used expression, known as the Weibull distribution, is the one developed in 1933 by Rosin and Rammler [2]:

$$1 - Q = \exp\left(-\left(\frac{D}{X}\right)^q\right) \tag{8}$$

Where Q is the fraction of the total volume contained in drops of diameter less than D, and X and q are constants. In particular, q indicates a measure of the spread of drop sizes, higher is q the more uniform is the spray, so, theoretically, if q is infinite all the drops have the same diameter. Usually, for most sprays the value q lies between 1.5 and 4.

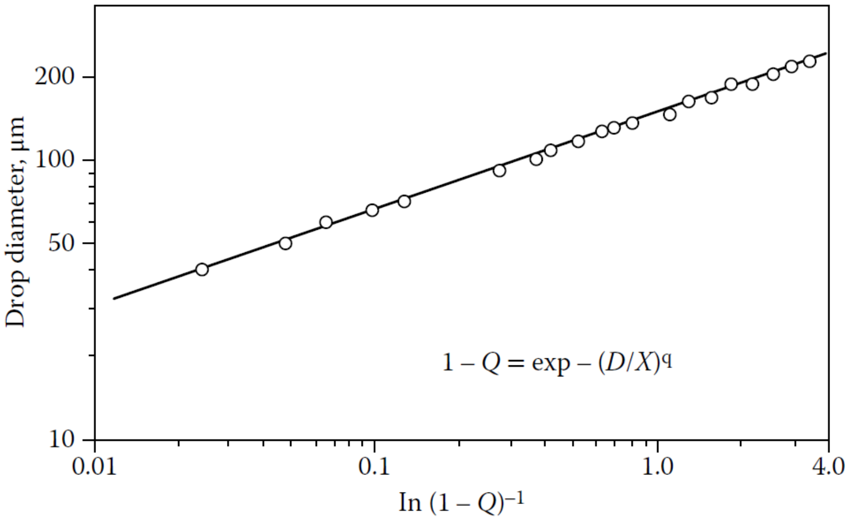

Figure 6 *Example of Rosin-Rammler plot.*

The droplet size distribution is commonly quantified with the Sauter Mean Diameter (SMD), which represents a measure of the volume to surface area ration of an average droplet within a given spray:

$$SMD = \frac{\sum N_i D_i^3}{\sum N_i D_i^2} \tag{9}$$

Where N_i is the number of droplets with the diameter D_i (μm).

2.5 Atomizers

Several types of atomizers have been developed so far, but essentially what is needed is a high relative velocity between the liquid to be atomized and the surrounding air or gas. Some atomizers obtain this effect by discharging the liquid at high velocity into a relatively slow-moving stream of gas. Others, on opposite discharge the liquid at slow velocity into a relatively high-velocity airstream.

Basically, the main types of atomizers are pressure atomizers **Figure 7(a)**, rotary atomizers **Figure 7(b)**, and twin-fluid atomizers **Figure 7(c)**.

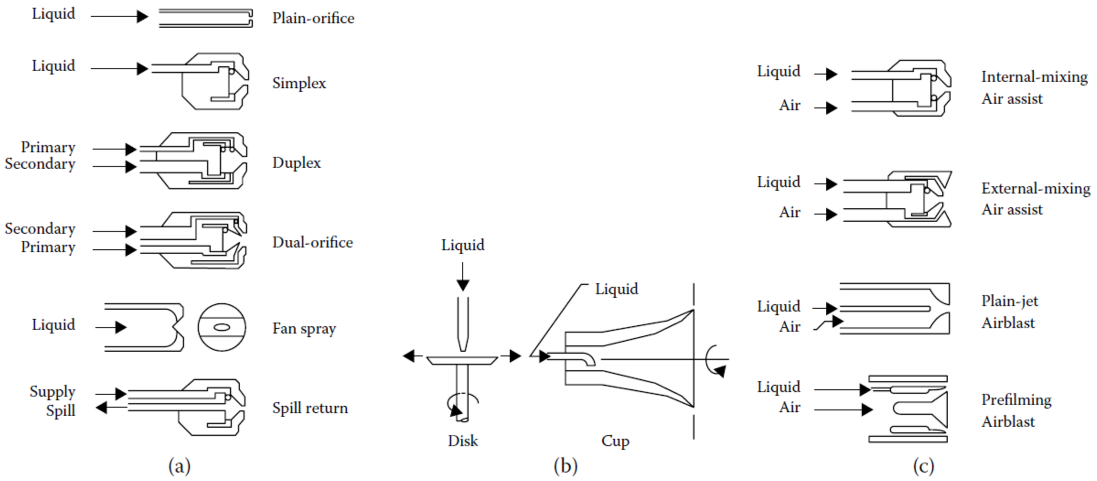

Figure 7 *(a) pressure atomizers, (b) rotary atomizer, (c) twin-fluid atomizers.*

2.5.1 Pressure atomizers

Basically, a pressure atomizer has a small aperture from where a liquid under high pressure is discharged, during this process the pressure energy is converted into kinetic energy (velocity). The exit velocity of the liquid is proportional to the square root of the pressure[2].

The simplest pressure atomizer is the plain orifice type, where a simple circular orifice is used to inject a liquid round jet into the surrounding air. The smaller is the orifice the finer is the atomization, anyway usually the orifice diameter are not smaller than 0.3 mm.

Another widely used pressure atomizer is the pressure-swirl type. In this configuration the circular orifice is preceded by a swirl chamber, the liquid flows towards the swirl chamber through some tangential holes or slots creating a core of air, then it emerges from the discharge orifice as an annular sheet, which continues to spread forming a hollow conical spray. The angle spray can vary from 30° to 180° based on the application. A finer atomization is obtained at high delivery pressure and with a wide spray angle.

The spill return type is another common atomizer, essentially it is an enhanced version of a simple nozzle but with a return flow line at the section back of the swirl chamber and a valve to control the amount of liquid injected outside the nozzle. With this configuration the supply pressure can be keep constant at a high value and the flow rate controlled by the spill return line without affecting the god atomization quality.

Some examples of other types of pressure atomizers that have been developed so far are the square, the duplex and fan spray.

2.5.2 Rotary atomizers

Typically, the rotary atomizers consist of a high-speed rotating disk with a system for introducing the liquid at its centre. Then the liquid leaves the centre flowing radially outward across the disk and being discharged at high velocity from the outer edge of the disk. Usually, at low flow rate, droplets are formed near the periphery of the disk, but at high flow rate at first ligaments and sheets are generated and, lately, these are disintegrated into droplets. A spray with quite uniform size is produced by small disk operating at high speeds.

Rotary atomizers result more flexible than pressure ones because of the independent variation of flow rate and disk speed.

2.5.3 Twin-fluid atomizers

The main characteristic of twin-fluid atomizers is that the liquid is exposed to an air stream flow at high velocity. In this category are included the air assisted and air blast atomizers, which can be divided into internal-mixing or external-mixing configuration.

As suggested by the name, in the internal-mixing air assisted atomizers the air and the liquid are mixed before being discharged out of the nozzle. The maximum spray angle is limited to 60° and energetically speaking it can result to be energy inefficient, but on the other hand it can produce a spray finer than the one produced by a simple pressure atomizer. In the external-mixing configuration the liquid and air are mixed outside the liquid discharge orifice.

By a comparison between these two configurations of air-assisted atomizers, in the external one there is no internal communication between gas and liquid, so problems of back pressures are avoided. Anyway, to reach the same degree of atomization, for the external one, a higher air flow rate is required. Nevertheless, both types of nozzles are good enough to atomizer high-viscosity liquids.

Air assisted and air blast nozzles are quite similar, but the main difference is that air blast one uses a larger amount of air flowing but a lower velocity, less than 100 m/s. Because of its characteristics air blast nozzles are widespread for atomizing liquid fuels in continuous-flow combustion systems, such us gas turbine.

Additional atomizers that can be mentioned are the electrostatic, the ultrasonic, the sonic and the windmill ones.

2.6 Influence of Liquid and Air Properties on Atomization

The quality of the atomization depends not only on the size and geometry of the atomizer but also on the physical properties of the liquid to be atomized (the dispersed phase) and the gas into which the droplets are discharged (the continuous phase).

The main three fluid physical properties that influence the atomization performances are the density, the viscosity, and the surface tension.

The influence of density on the mean drop size is quite small because most of liquids exhibit minor differences in this property [2].

The surface tension is important because it represents the force that resists the formation of new surface area. Basically, the surface area before the break-up is that of the liquid cylinder emerging from the nozzle, but after atomization the surface area is the sum of the surface of all the single droplets. The minimum energy required for atomization is equal to the surface tension multiplied by the increase in liquid surface area. To have an idea of typical surface tension values, it can vary from 0.073 $\frac{\mathrm{kg}}{\mathrm{s}^2}$ for water to 0.027 $\frac{\mathrm{kg}}{\mathrm{s}^2}$ for petroleum products and generally the surface tension decreases with an increase in temperature [2].

The fluid viscosity has a relevant impact not only on the drop size distribution of the spray but also on the spray pattern and on the nozzle flow rate. An increase in viscosity lowers the Reynolds number and hinders the development of any natural instability in the jet or sheet.

At high viscosities, however, the flow rate usually diminishes with increasing viscosity. With pressure-swirl nozzles, an increase in viscosity generally produces a narrower spray angle. At very high viscosities the normal conical spray may collapse into a straight stream of relatively large ligaments and drops.

The viscosity of these liquids ranges from 0.001 kg/m·s for water to0.5 kg/m·s for heavy fuel oil. The viscosity of liquids generally decreases with an increase in temperature. It is customary to heat up many of the heavier fuel oils, partly to reduce pumping power requirements but also to improve atomization.

3. **Fast Pyrolysis Bio-oil**

Pyrolysis oil can be considered as a promising and economical alternative to fossil oils. However before to reach this point, due the different chemical composition and physical properties compared to standard fuels, atomization and combustion characteristics need to be widely discussed. Moreover, pyrolysis bio-oils can be obtained from different biomass feedstocks, and its characteristics are strongly depended on the composition of the biomass feedstock, the type of pyrolysis process, the post-production upgrading and the age of the sample.

3.1 Pyrolysis technologies

Pyrolysis oil is obtained from a thermal decomposition process, called ‘’pyrolysis’’, which takes place at atmospheric pressure in absence of oxygen, and which converts lignocellulosic biomass into carbon-rich solids and liquids. The main components of lignocellulosic biomass are lignin, cellulose, and hemicellulose, they produce *biooil, biochar and syngas* if thermally degraded at 300-500°C temperature range.

Pyrolysis process can be classified as slow, intermediate, fast, and flash, but the most commonly systems used are the slow and fast ones. The relative quantity of products and their composition depends on several factors, such as: feedstock type, temperature, particle size and process parameters (residence time, temperature, and heating rate).

Slow pyrolysis process occurs at moderate temperature, low heating rate and long residence time, and the main product is biochar. On the opposite, fast pyrolysis process produces mainly biooil, thanks to a rapid heating rate and short residence time. In other words, fast pyrolysis produces higher quality and quantity of biooil than slow pyrolysis [5][6][7].

Generally, pyrolyzer is made of a reactor, a cyclone, and a condenser. Biomass is fed into the reactor and converted into different products through several thermochemical reactions. The cyclone divides solid products from liquids and gases. After that, the vapor products are rapidly quenched in the condenser and the biooil is separated from other gases. Additionally, catalysts can be used with biomass to improve the conversion efficiency or to upgrade its products into more precious products [8].

Different types of reactors can be used on the base of the pyrolysis process. In the case of slow pyrolysis drum, rotary kilns and screw/auger are the most used. In fast pyrolysis systems the most common reactors are fluidized bed, vacuum, entrained flow, rotating cones, and ablative.

Process	Reaction temperature [°C]	Heating rate [°C/s]	Residence time	Feedstock size	Product yield, %		
					Biooil	**Biochar**	**Gas**
Slow pyrolysis	300 - 550	0.1 - 0.8	5 – 30 min; 25 - 35 h	Briquette/ whole	20 - 50	25 - 35	20 - 50
Intermediate pyrolysis	300 - 450	3 - 5	~ 10 min	Coarse/ chopped/ finely ground	35 - 50	25 - 40	20 – 30
Fast/Flash pyrolysis	300 - 1000	10 - 1000	< 2 s	Finely ground	60 - 75	10 - 25	10 – 30

Table 1 *Overview of pyrolysis parameters and product yields for various technologies.*

3.1.1 Slow pyrolysis

Slow pyrolysis is used to produce biochar/charcoal. The process consists of a low heating rate and long residence time at temperature in the rage of 300-550 °C (Table 1).

Using this process, biooil and biochar yields depend on the feedstock properties and operating temperature, biochar yield decreases with increasing temperature. Anyway, there is not a clear dependence between the heating rate and the yields.

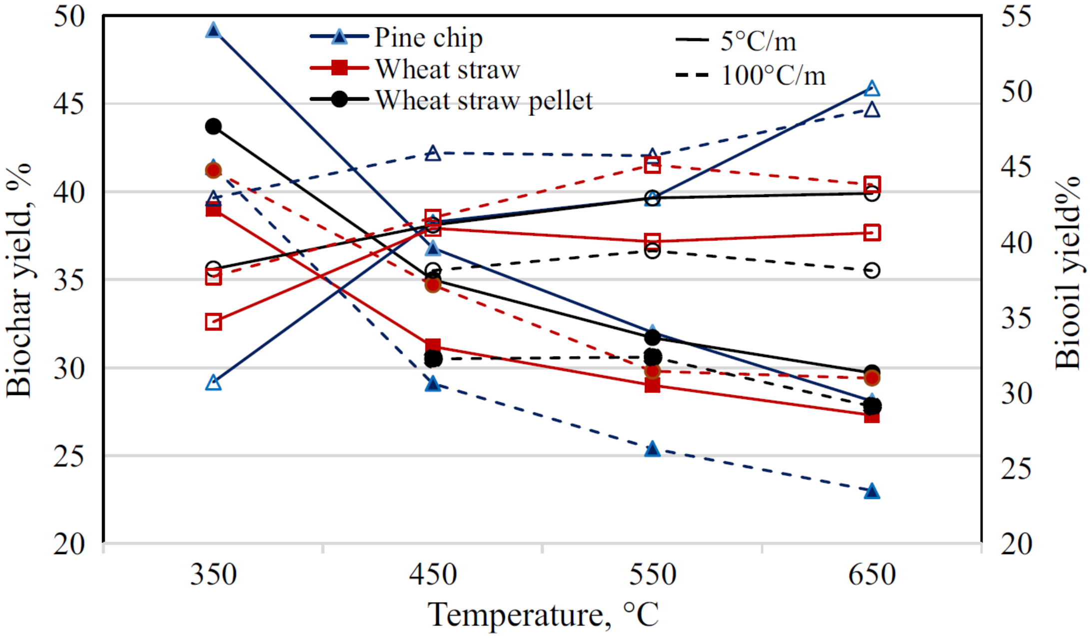

Figure 8 *Effect of pyrolysis temperature and heating rate on biochar and biooil yield (biochar: solid symbols; biooil: open symbols).*

3.1.2 Fast pyrolysis

In fast pyrolysis process, volumes of biooil around 65-80% are produced by very high heating rate for a very short residence time (Table 1).

Pyrolysis parameters and the feedstock properties can have a significant impact on the biooil yield. Generally, woody biomass, such as forest residues, poplar, or sawdust, produces the highest biooil yield. Energy crops and agri-residues produce also high yields of biooil.

In the case of fast pyrolysis process, another importance factor that affects the product yields, is the feedstock particle size. Increasing the particle size, the heat transfer rate decreases and biooil and syngas yields decrease. This means that biooil yields can be maximized by optimizing pyrolysis temperature and feedstock particle size.

3.2 Fast pyrolysis bio-oil properties

Fuel properties	Method	Diesel fuel (EN 590 98/70/EC)	Denatured ethanol	Filtered FPBO
C [wt%]	ASTM D5291	86.5	44.93	54.97
H [wt%]	ASTM D5291	13.5	12.30	6.43
N [wt%]	ASTM D5291	0	0.02	0
S [wt%]	Internal method	<0.0001	0	0.013
O [wt%]	Calculated	<2.7	42.7	38.56
pH	ASTM E70	-	7	2.7
Ash content [wt%]	EN ISO 6245	-	0	0.02
Water content [wt%]	EN ISO 8534	-	7.2	22.5
Kinematic viscosity at 313 K [$mm^2 s^{-1}$]	EN ISO 3104	2-4.5	1.1	37.01
Density at 298 K [$Mg m^{-3}$]	EN ISO 3675	0.82-0.85	0.817	1.192
Solid content [wt%]	ASTM D7579	0	0	0.0197
HHV [$MJ kg^{-1}$]	DIN 51900-2	45.60	25.37	18.91
LHV [$MJ kg^{-1}$]	Calculated	42.50	22.76	17.32

Table 2 *Chemical characterization of fuels* [9]**.**

Characterization of FPBO is not so easy because of its composition, made of several groups of compounds with different polarity and wide range of boiling points and molecular weights.

FPBO’s chemical composition contains aromatic and aliphatic hydrocarbons containing carboxylic acid and hydroxyl groups, commonly in the form of various substituted phenols and furanoics, which are emulsified with varying amounts of water. FPBO is also highly polar, due to its high content of oxygen, about 35-45 wt%, consequently it is not soluble in mineral oils or other biooils, such as biodiesel.

Generally, FPBO has high water content, a density higher than standard fossil fuels, a low heating value and can have levels of suspended solids. It is high viscous and if heated too much (over 80°C) it is predisposed to polymerise.

With the premise that physicochemical properties of FPBO change based on the feedstock, processing, upgrading and age, the following part presents a general overview of its typical properties that most affect atomization and combustion [6].

3.2.1 Particle size distribution

To determine the particle size distribution different methods can be used, the optical microscopy analysis and the particle size laser analysis are two of them. In the first one, the sample is diluted in ethanol and thanks to an automatic particle counter, particles larger than 5 μm are revealed. Anyway, the dark colour of the sample can disturb the detection and in addiction if some particles are overlapped, they can be reported as only one large particle.

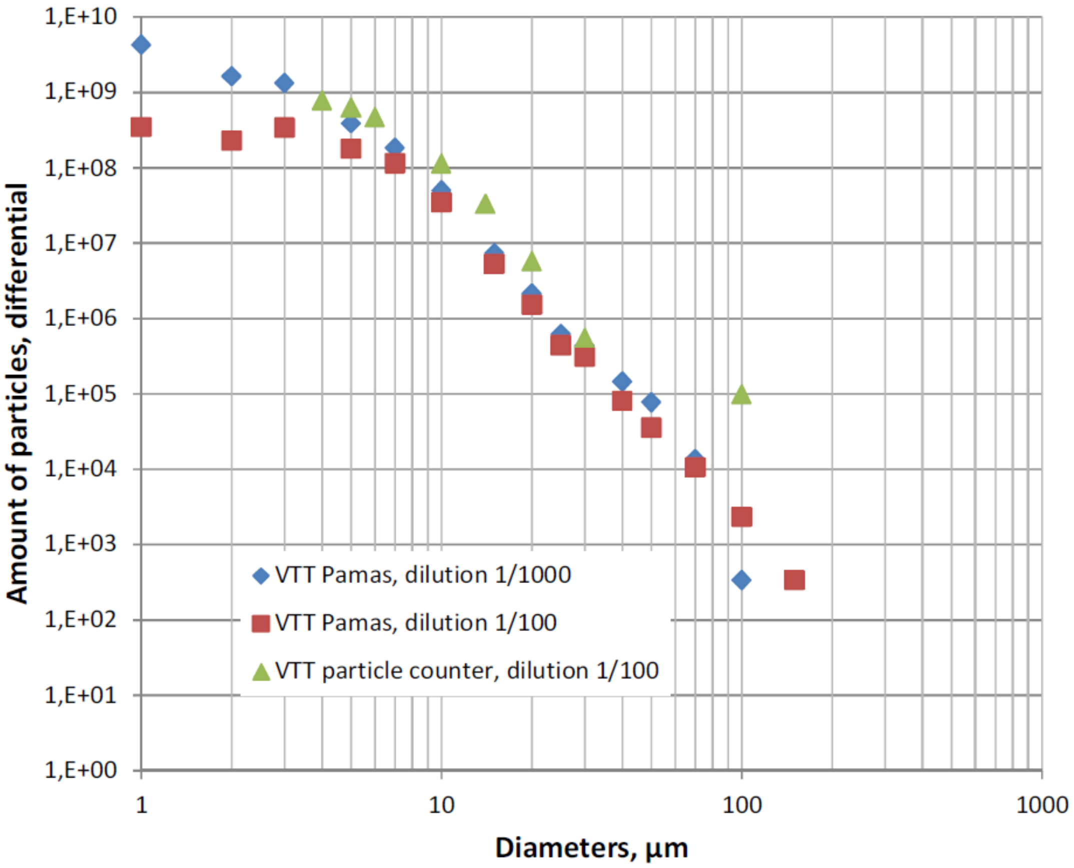

***Figure 9** The particle size distribution for one fast pyrolysis bio-oil (solids content 0.33 wt%) using two optical particle counters and two dilutions.*

The second method works in a different way, in fact, a sample is located between two glass plates and through a video camera, that is connected to a polarisation microscope, pictures are taken. These pictures are later elaborated by an image analyser and so the particle size distribution is obtained.

Nevertheless, similar results have been found using both the methods. In the **Figure 9** is reported the particle size distribution supplied by VTT, as can be easily read by the graph most of the particle are below 10 μm [6].

3.2.2 Water content

The water content in petroleum fuels is a problem because it forms a separate phase that can result in corrosion, emulsion formation and problems in burners, for this reason usually the amount of water is adjusted.

In FPBO there is also a relevant water content, and typically it is high (more than 20 wt%), but unlike petroleum fuels, water is either dissolved or else it exists as a microemulsion, so that its removal by physical methods is not possible. The water content affects the fuel properties as well as the phase stability, so it must be properly regulated.

Large amount of water affects FPBO properties as density, viscosity and heating value and improves the stability of the bio-oil up to it starts to separate out, usually when the water content is above 30 wt%.

On one hand, high-water content has negative consequences, it results in low energy density, lowers adiabatic flame and local combustion temperature and in addition low combustion reaction rates and high specific heat in the vapour phase. Moreover, it causes troubles in ignition, increases the ignition delay time and in case of preheating, high water content, can lead to the premature evaporation of water and other low-boiling components, inducing in some undesired effects in the fuel line.

On the other hand, the present of water can be positive, it improves the properties of the FPBO by reducing the viscosity and it also reduces the NOx emissions by reducing the flame and local temperature in the combustor chamber. In any case, too high amount of water can be dangerous for the flame stability and controllability of the combustion [6][7].

3.2.3 Oxygen content

FPBO has a high oxygen content, it is around 35-40% (dry basis) and contained in most of the 300 compounds that formed the bio-oil. Obviously, the original feedstock and the production process affect the distribution of these compounds.

One of the consequences of the high oxygen content is that the FPBO is immiscible in fossil oils, which are not oxygenated. Moreover, this factor is responsible for the fuel's low energy density, corrosivity and chemical instability and aging. On the other hand, a positive consequence is that during the combustion a lower amount of air is needed, this means a low air/fuel ratio, and so this also reduces the amount of flue gases generated.

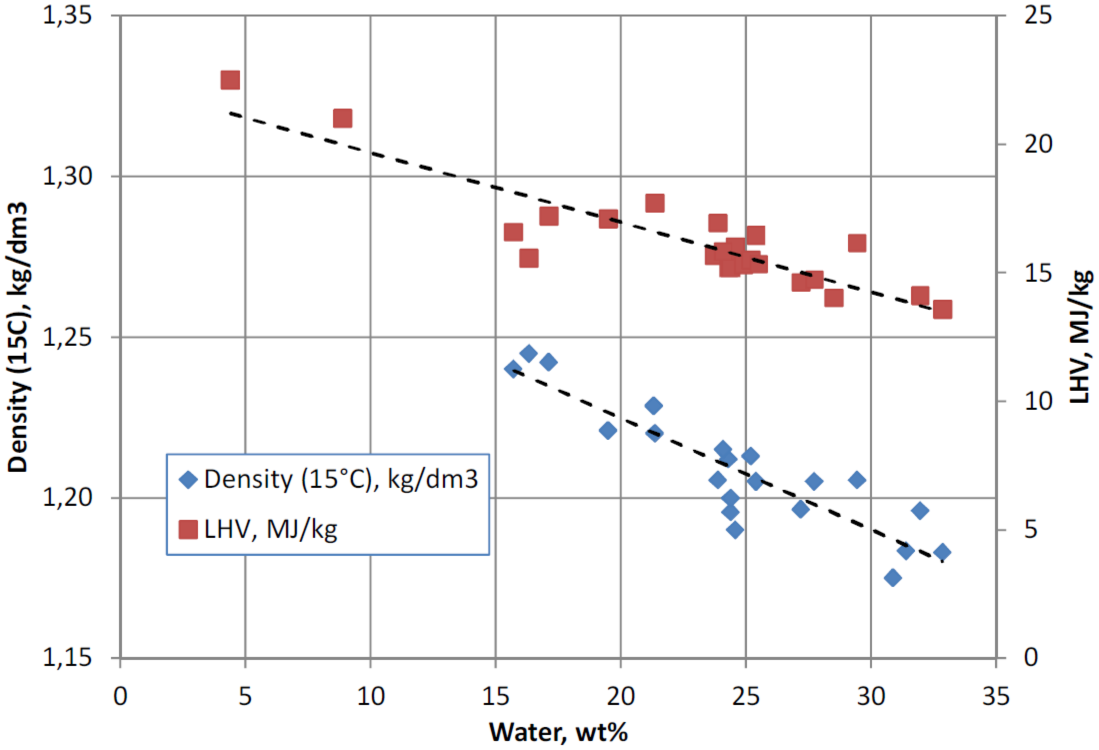

__Figure 10__ Density and heating value of pine and forest residue pyrolysis bio-oils as a function of water content.

On the other hand, a positive consequence is that during the combustion a lower amount of stochiometric air is needed, this means a lower air/fuel ratio during the combustion, an increasing flame temperature and reduced amount of flue gases generated [6].

3.2.4 Density, viscosity, and surface tension

Density, viscosity, and surface tension are some of the most significant parameters influencing the combustion of FPBO. They can impact pump and pipeline design and especially the atomization quality of the spray injectors, as consequence of this also the efficiency of combustion and emissions is ruined. As larger are these parameters as larger is the droplet diameter distribution emitted from the injector nozzle and so the vaporization, ignition and combustion of the droplets are negatively affected.

The surface tension of a liquid is a property that permits it to resist an external force. In literature typically values of surface tension varies in a range of 31-40 mN/m at room temperature (25°C) and drop about 5 mN/m at 80°C. FPBO’s surface tension depends on the water and char content, for this reason it is higher than the values of surface tension of heavy and light fuel oils, 23 mN/m at 40°C and 28 mN/m at 25°C respectively, which, in fact, contain no water.

Viscosity is a measure of a fluid's resistance to flow, so that FPBO can be considered as a high viscosity fuel, even more if compered to fuels such as diesel or gasoline. The viscosity of a fuel is usually measured as kinematic viscosity, nevertheless it can be determined also as dynamic viscosity, using rotational viscometers. These two different viscosities are correlated by the following equation:

$$\nu = \frac{\eta}{\rho} \tag{10}$$

where:

ν is the kinematic viscosity (cSt) at temperature T,

η is the dynamic viscosity (mPa s) at temperature T,

ρ is the density (kg/l) at temperature T.

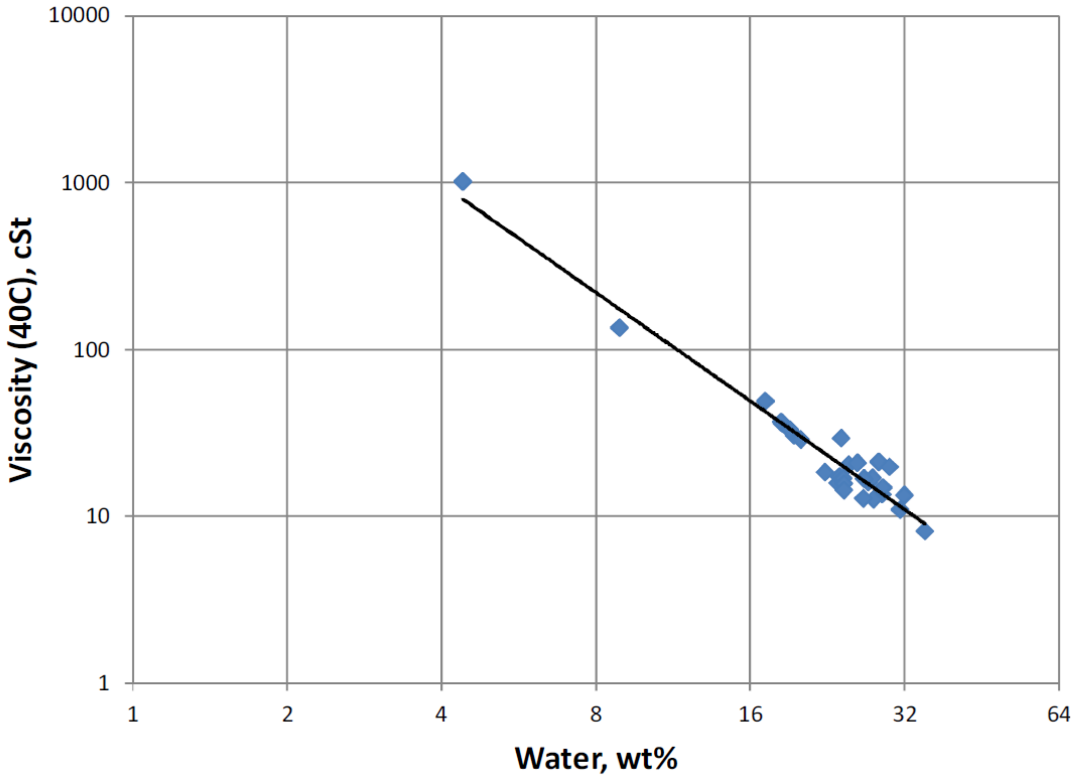

Figure 11 *Viscosity of pyrolysis bio-oils from pine and forest residue as a function of water content.*

Another relevant parameter is the pour point of the fuel, it indicates the lowest temperature at which the fuel can be pumped. The advised upper limit for pumpability is around 600 cSt.

Another relevant parameter is the pour point of the fuel, it indicates the lowest temperature at which the fuel can be pumped. The advised upper limit for pumpability is around 600 cSt.

Lastly, the density of FPBO is about 1.2 kg/dm at 15°C for a water content more or less of 25 wt%. It is interested to notice that FPBO’s density is about 40% higher than that of fossil oils [5][6][7].

3.2.5 Heating value

The heating value of a fuel is the amount of heat released during the complete combustion of a specified amount of it. This parameter can be defined in two different ways, the higher heating value (HHV), indicated as the gross and the lower heating value (LHV), indicated as the net, the difference is equal to the heat of water vaporisation formed by the combustion of the fuel.

The LHV can be calculated from the HHV and hydrogen content by the following equation:

$$LHV = HHV \ - 218.13 * \ H \ (wt\%) \ \left[\frac{J}{g}\right] \tag{11}$$

The heating value of FPBO oil is less than half (of a dry organic basic) of that of petroleum fuels.

With respect to combustion systems, which operate with conventional fossil fuels, a lower heating value results in a higher flow rate of FPBO for the same fixed energy throughput. This means that combustor need modifications, especially the nozzle and injection system to maintain suitable atomization and fuel/air mixing. Furthermore, the sizing of tanks, piping and also the solutions for transport have to take into account the characteristics of the bio-oil.

Generally, the adiabatic flame temperature of FPBO is about 1400 - 1700 °C which is slightly lower than that of traditional petroleum fuels 1700 - 2000 °C [6].

3.2.6 Volatility and ignition properties

FPBO can be classified as a non-flammable and non-distillable, it has a limited volatility and ignite only at high temperatures. This behaviour is in contrast with classic mineral oils.

The flash point of a fuel is the maximum temperature at which it can be stored and handles without fire risk. In the case of FPBO, it has been measured that the flash point ranges from40°C to above 100°C.

The explanation of this attitude lies in its chemical composition, in fact, in FPBO there are some light compounds (typically below 5 wt%) that evaporate at approximately ambient temperature and can cause a short-duration flash in presence of heat and air. Among these components are included acetaldehyde, acetone, and methanol. In any case, thanks to the large amount of vapour, the flash is quickly suppressed.

Another relevant difference with mineral oils is that FPBO in not such thermally stable since cracking already takes place below 100 °C and is intensified by temperature and coke formation can be up to 50 wt%. This behaviour contrasts with conventional petroleum fuels, such as diesel, which has a 10–90 wt% distillation between 220–300 °C [6][7].

3.2.7 Thermal and electrical conductivity, specific heat capacity

Thermal conductivity and specific heat capacity are crucial in the design and evaluation of transport units and sizing apparatus, such as atomizers and combustors.

Thermal conductivity of 0.39 W/mK over the temperature range 44–63 °C has been determined by Peacocke et al. and Qiang et al.

Electrical conductivity is not a property directly used to fuel applications, anyway it is needed by some instruments for measurement and control function. There is not much published data available on the electrical conductivity of FPBO.

Specific heat capacity of bio-oil value has been 2.8–3.2 kJ/kg K (±300 J/kg K) over the temperature range of 26–61 °C [6].

3.2.8 Solid, ash, carbon residue, metals

Usually, FPBO contains less than 1.0 wt% of solids which include organic char and, in part, inorganic ash that cannot be burned. On average the diameter of the solid particulate is 5-10 µm and smaller than 3 µm for the 50% of particulate; large particles are removed using cyclones during the pyrolysis process.

The inorganic solids have more than one negative effect on bio-oil as a fuel, for example the agglomeration of particles during the storage with the consequent formation of a slim layer on the bottom of the container and the increase of the rate oil ageing. They can also affect erosion in the pumps and cause clogging, erosion, and coke residue deposition, all of which lead to troubles with the longevity, reliability and functionality of the fuel injection system and combustor.

The present of char content speeds up the occurrence of micro-explosions which are not very effective at the shattering of the original fuel droplet. In terms of fuel handling, storage, stability, atomization quality and combustion behaviour, bio-oil with a low content of char are preferred [6].

3.3 Applications

As already said, FPBO finds application in burners, boilers, furnaces, as well as gas turbines and compression-ignition engines.

Burners, boilers, furnaces fit well with the unconventional FPBO properties. In fact, usually, these types of devices are less sensitive to the fuel atomization, fuel-air mixing or combustion characteristics because of their long residence time and versatile designs.

Several tests have been conducted on these applications, showing good combustion results and emissions within acceptable limits.

Generally, gas turbine combustors can be divided into two categories: annular and can. Annular combustors are widely used in aero engines, while can combustors are commonly installed in heavy-duty frame engines. Usually, gas turbines work with light fuel oils, such as kerosene or diesel, which are atomized by pressure-swirl or air-blast atomizers. Tough, it is believed that with the correct adjustments, gas turbines could operate with FPBO. The problems to face in this case are the flame instability, the inadequate fuel residence time, and the incomplete combustion, which lead to an increase in PM and gaseous emissions and coke/char residue deposition [5].

An important contribution to this topic has been given with the research work of M.Buffi et al., of which one of the most interesting experimental works deals with the combustion of FPBO in micro gas turbines [9]. In this study a gas turbine test ring was developed with several new components, which include a new re-designed combustor. Moreover, the tests have been run out with FPBO and EtOH blends at 20/80 and 50/50%.

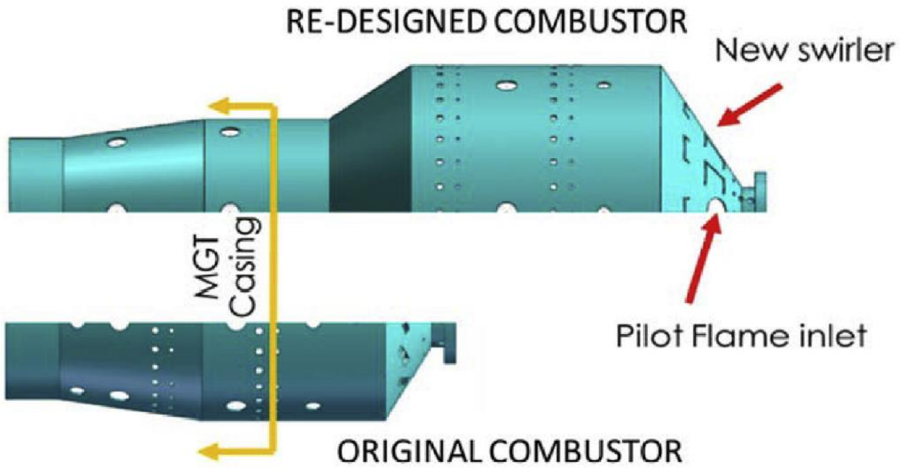

Figure 12 *3D model of the new combustor (top) versus the original Garrett GTP 30–67 model (bottom).*

As shown in **Figure 12** the new re-designed combustor is larger than the original one, with this new configuration it has been noticed an improvement on the quality of the combustion and a reduction in the CO emissions. This effect is due to the longer residence time and a better distribution of air along the liner. Finally, it has been shown that, increasing the volume fraction of FPBO in the composition of the blend, the CO emissions increase because of the formation of larger droplets. While NOx emissions increase because of the fuel-bound nitrogen.

In conclusion, even if industrial scale gas turbines have been developed to work with FPBO, long term operation has not been reported yet due to the challenges associated with the spray combustion of FPBO in these engines [5].

4. **Atomization of FPBO**

Atomization is one of the most critical aspects of liquid fuel combustion, in fact, a better atomization makes possible performing a more efficient combustion and reducing the emissions. Smaller droplets mean a larger relative surface area and so a more rapid heat transfer and an increased vaporization. An intensified vaporization improves the air/fuel mixing and ignition and reduces the necessary fuel droplet residence time and so the flame length.

The atomization quality mainly depends on three fuel properties: viscosity, surface tension and density. Generally, for light fuel oils simple pressure or pressure swirl atomizer are enough to generate droplets in the range of 20-60 μm, while for more heavy fuel oils twin-fluid or rotating cup atomizer are preferred and to obtain droplets in the range of 50-70 μm, usually, the heavy fuel oils are preheated to 85-140°C. However, when FPBO is preheated over 80°C, polymerization, nozzle clogging and severe fuel quality degradation can occur [5].

It has been shown in several experiments that twin-fluid atomizers provide a better atomization for FPBO than the one obtained with pressure ones.

Kyle Redfern, in his thesis work, studied the performance of pyrolysis oil in a large-scale combustion system, with particular application for building heating boilers [10].

As first attempt a pressure atomizer has been used, later an air assisted atomizer, both provided by Delevan. The pressure atomizer was a WDA model, these nozzles are designed to work at an operative pressure of 100 psi and produce a hollow cone with a spray angle of 70°. The air assisted atomizer was an AIRO model, rated for a range of flows up to 60 gph and to generate a solid cone spray, with a variable spray angle.

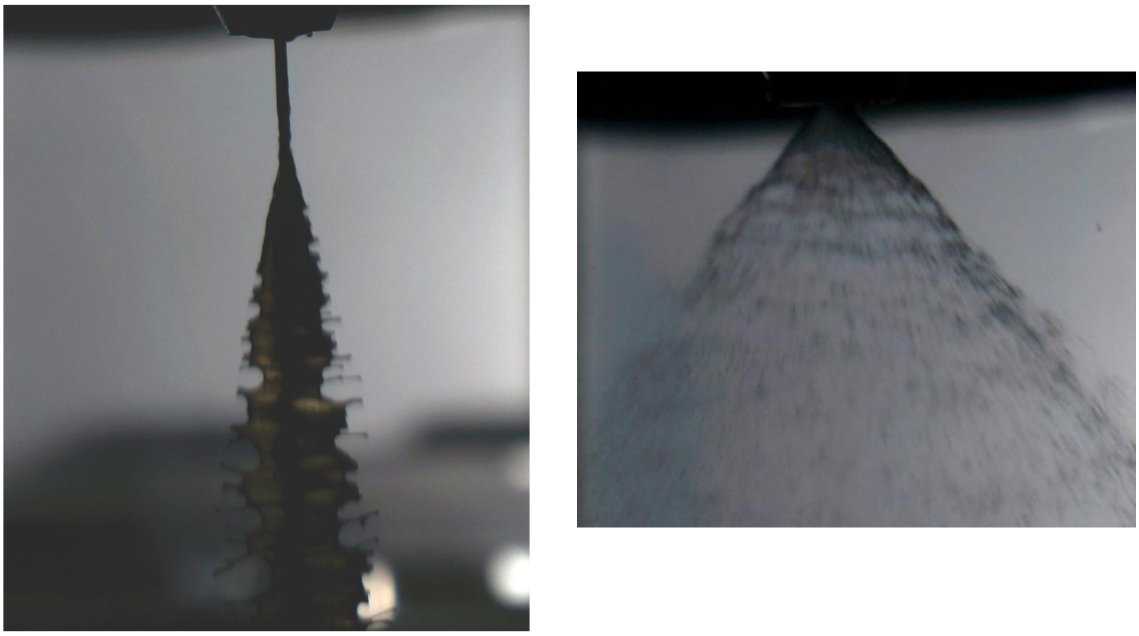

***Figure 13** Pressure atomized spray of 80:20 FPBO:EtOH at 100psi (left) and Pressure atomized spray of water at 100psi (right)*

The pressure atomizer was set up to work with a blend of 80% of FPBO and 20% of EtOH and an operating pressure of 100psi. The result is shown in the **Figure 13,** where is visible that the spray is a simple jet and not a hollow cylinder structure as expected. To have a comparison the same test has been performed with water, showing that with a low-viscosity liquid the pressure atomizer is able to achieve a good atomization.

Therefore, pressure atomization of FPBO is challenging task because of the risk of clogging and erosion due to the fuel particulates and the small orifices of nozzles, which are necessary to reach so high pressures. Moreover, the high pressure required to obtain fine droplets of FPBO combined with the high viscosity of the oil makes the pumping of the fuel not so easy.

Different results have been obtained using an air assisted nozzle. As shown in the **Figure 14** an acceptable atomization is achieved, with an atomizing air at 25psi there are still large droplets and long ligaments but increasing the pressure at 35psi this undesirable effect is avoided more homogeneous droplet spray is generated.

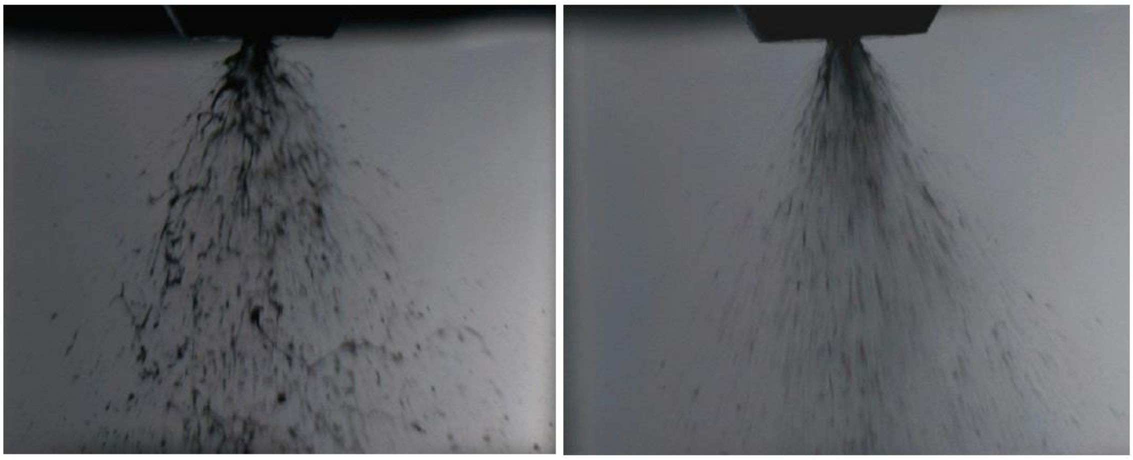

Figure 14 *Air assisted atomization of 80:20 FPBO:EtOH at 25psi(left) and 35psi(right).*

Established that twin-fluid nozzles, which are less sensitive to the fuel properties, are more suitable for operating with FPBO, can be useful understand which configuration between internally and externally mixing is better to atomize FPBO. Generally, it has been shown, that the internally-mixing configuration is the more effective for FPBO and so it is the best option for FPBO atomization.

About this topic different studies have been published, for example the one of M. Broumand et al. where they tested two twin-fluid nozzle, one externally mixed and one internally mixed, with the same equivalent orifice diameter of 1.44mm. The externally one was a nozzle used in the commercial diesel fired 30 kW Capstone gas turbine and the internally one was supplied by BEX Spray Nozzles. Thanks to a laser-diffraction-based instrument the droplets size (SMD) has been evaluated [11].

The range of air-to-liquid mass flow ratio ($ALR = \frac{\dot{m}_a}{\dot{m}_l}$) was fixed between 0.25 and 0.65 and as easy predictable higher ALR values reduced the spray SMD, and more in detail the internally mixed nozzle exhibited a greater rate of decrease in SMD with increasing ALR. Moreover, at high ALRs, the internally mixed nozzle produced a smaller SMD than the of generated by the externally mixed one and this result is consistent with the other studies reported in literature which mention that externally mixed nozzles are less efficient than internally mixed ones.

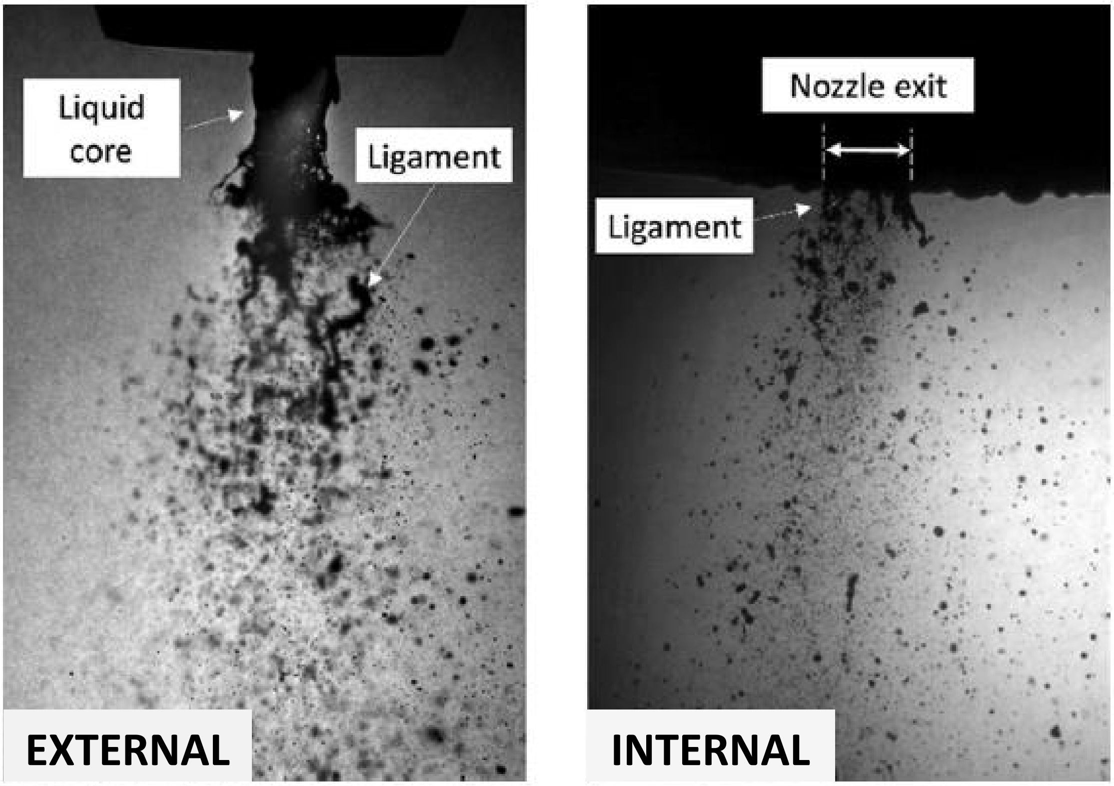

Figure 15 Shadowgraph images of water atomization using (left) an externally mixed nozzle and (right) an internally mixed nozzle.

The different spray SMD production between the externally mixed nozzle and the internally mixed one is attributed to their distinct atomization mechanisms, namely classical and prompt atomization, respectively. The externally mixed nozzle features centreline injection of a liquid jet surrounded by a high velocity airflow which forces the formation of the waves that consequently leads to the jet disintegration into droplets. On the opposite side, the liquid jet in the internally mixed nozzle has no time to develop a wavy structure but is immediately destroyed into fragments by its interaction with atomizing air at an appreciable air-liquid relative velocity and/or impingement angle inside the nozzle. An essential feature of the prompt atomization is that the rapid disruption of the liquid jet creates smaller droplets, whereas the presence of an intact liquid core and large ligaments in the near nozzle region in classical atomization degrades the jet’s atomization quality, see Figure 15 [11].

5. **CFD**

Computational fluid dynamics or CFD is the analysis of systems involving fluid flow, heat transfer and associated phenomena by means of computer-based simulation. The technique is very powerful and covers a wide range of industrial and non-industrial application sectors. Recently, methods have been applied to the design of internal combustion engines, furnaces, and combustion chambers of gas turbines. In addition, car manufacturers now routinely predict drag forces, under-bonnet air flows and the in-car environment with CFD. Increasingly CFD is becoming a fundamental element in the design of industrial products and processes.

The cost of an experiment, in terms of hourly-person costs and/or facility hire, increases with the number of data points and the number of configurations tested. Contrary, CFD codes can produce extremely large volumes of results without additional expense, and it is very economical to perform parametric studies, to optimize equipment performance.

CFD codes are structured around numerical algorithms that can solve fluid flow problems. To provide easy access to their solving power all commercial CFD packages include sophisticated user interfaces to input problem parameters and to examine the results. Hence all codes contain three main elements [1]:

- a pre-processor
  This step includes a definition of the computational domain, a grid of cells, the selection of the physical and chemical phenomena that need to be modelled, the definition of the fluid properties and the specification of the boundary conditions.
  The solution to a flow problem is defined at nodes inside each cell. The accuracy of a CFD solution depends on the number of cells in the grid and generally, it improves increasing the number of cells. Both the accuracy of a solution and its cost in terms of necessary computer hardware and calculation time are dependent on the fineness of the grid. Optimal meshes are non-uniform: finer in

areas where large variations occur from point to point and coarser in regions with relatively little change.

- a solver

  There are three distinct streams of numerical solution techniques: finite difference, finite element, and spectral methods. The most applied is the finite volume method, a special finite difference formulation. Briefly this numerical algorithm consists of the following steps: the integration of the governing equations, the discretisation (conversion of the resulting integral equations into a system of algebraic equations) and the solution of the algebraic equations by an iterative method.
- a post-processor

  In this last step different data visualisation tools are involved, such as: domain geometry and grid display, vector plots, 2D and 3D surface plots, particle tracking and so on.

5.1 Governing Equations of Fluid Flow

The governing equations of fluid flow follow the conservation laws of physics:

- The mass of a fluid is conserved,
- The rate of change of momentum equals the sum of the forces on a fluid particle (Newton’s second law)
- The rate of change of energy is equal to the sum of the rate of heat addition to and the rate of work done on a fluid particle (first law of thermodynamics)

The behaviour of the fluid is described in terms of macroscopic properties, such as pressure, velocity, temperature, density and their time and space derivatives. These are referred to each fluid particles, which are the smallest possible element of fluid whose macroscopic properties are not influenced by individual molecules.

Generally, the properties are computed in each small finite element with sides δx, δy and δz.

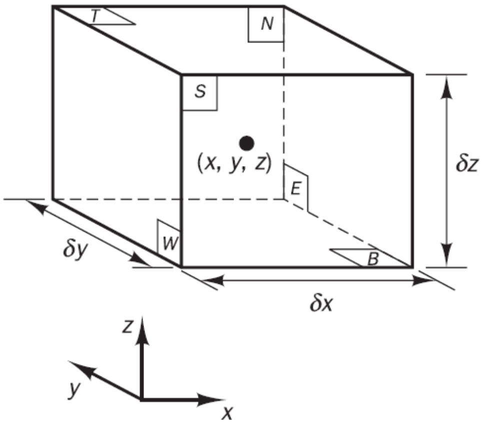

Figure 16 *Fluid element for conservation laws*

The general equations that govern the flow of fluids are the continuity equation, the Navier-Stokes equations and energy equation.

The continuity equation can be compactly expressed in vector notation as

$$\frac{\partial \rho}{\partial t} + \nabla \cdot (\rho \boldsymbol{u}) = 0 \tag{12}$$

Where the first term on the left-hand side is the rate of change in time of the density and the second term on the right-side is the net flow of mass out of the element across the boundaries (also called the convective term). The first term is equal to zero for incompressible fluid due to the constant density.

The Navier-Stokes can be written as

$$\frac{\partial}{\partial t}(\rho \boldsymbol{u}) + \nabla \cdot (\mathrm{\rho} \mathbf{uu}) + \nabla \cdot \mathrm{p} - \nabla \cdot \boldsymbol{\tau} - \mathrm{\rho} \mathbf{g} = 0 \tag{13}$$

Where τ is the deviatoric stress tensor and g the body accelerations, for examples gravity.

And finally, the energy equation can be expressed in function of the specific total enthalpy h_0

$$\frac{\partial}{\partial t}(\rho h_0) + \nabla \cdot (\rho h_0 \mathbf{u}) - \nabla \cdot \mathrm{q} - \boldsymbol{\tau} \cdot (\nabla \mathrm{u}) - \frac{\partial p}{\partial t} - S = 0 \tag{14}$$

Where q is the heat flux and S the source term.

5.2 Discretization Methods

Once the equations have been defined, the following step is the choice of the mathematical model, that is the set of partial differential or integral-differential equations and boundary conditions. After that the selection of a discretization method is needed.

The discretization is the process of transferring continuous functions, models, variables, and equations into discrete counterparts. There are different ways to approximate the flow variables: Finite Difference Method (FDM), Finite Element Method (FEM) and Finite Volume Method (FVM). Anyway, most of CFD codes are based on the last one, FVM.

The FVM is based on the integral form of the conservation and a solution domain that is divided into smaller control volumes (CVs). The conservation equations are applied to each these control volumes and the variable values are referred to the centroid of each CV. Following that, the solution for the entire domain is expressed thanks to interpolation.

The positive aspects of FVM are its suitability for complex geometries and that mass, momentum, and energy are automatically conserved since the integral forms of the governing equations are solved.

On the other hand, with FVM, methods of order higher than second are more difficult to develop in 3D than with FD schemes.

5.3 Turbulence Modelling

In engineering practice, all the flows, starting from the simple ones, such as two-dimensional jets or pipe flows, to the more complicated three-dimensional ones, become unstable above a certain Reynolds number:

$$Re = \frac{UL}{\nu} = \frac{[inertial\ forces]}{[viscous\ forces]} \tag{15}$$

where *U* and *L* are characteristic velocity and length scales of the mean flow and *v* is the kinematic viscosity.

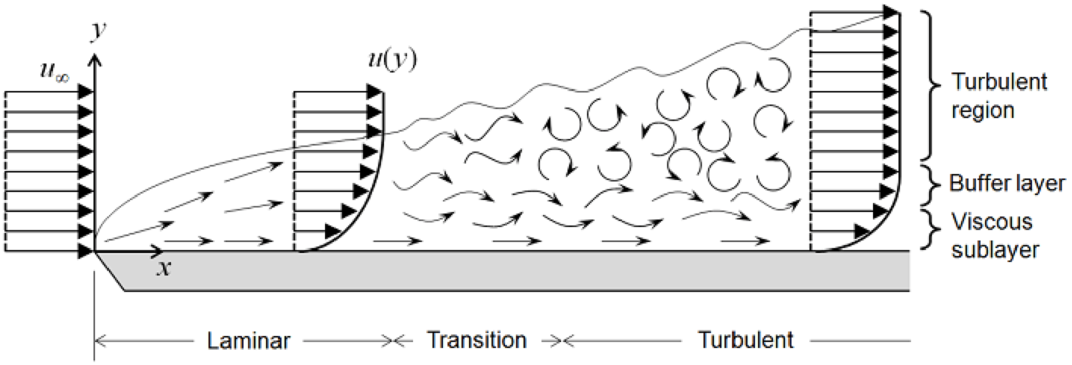

Figure 17 *Representation of laminar, transition, and turbulent flows*

The Reynolds number of a flow gives a measure of the relative importance of inertia forces (associated with convective effects) and viscous forces. Flows are laminar at low Reynolds and became turbulent at higher Reynolds numbers.

In experiments on fluid systems, it is observed that at Re values smaller than the so-called critical Reynolds number Re_{crit} the flow is smooth and the adjacent layers of liquid flow over one another in an orderly manner.

Moreover, the flow is defined steady if the applied boundary conditions are constant over time, this regime is called *laminar flow*.

On the opposite side, at values of Re above Re_{crit} a complicated series of phenomena occurs and can lead to a remarkable change of the flow character. In the final state the flow behaviour is chaotic and random. The motion becomes intrinsically unsteady even with constant imposed boundary conditions. This regime is called *turbulent flow*. Any way the chaotic nature of turbulent flows is useful to enhance applications such as mixing, heat and mass transfer processes.

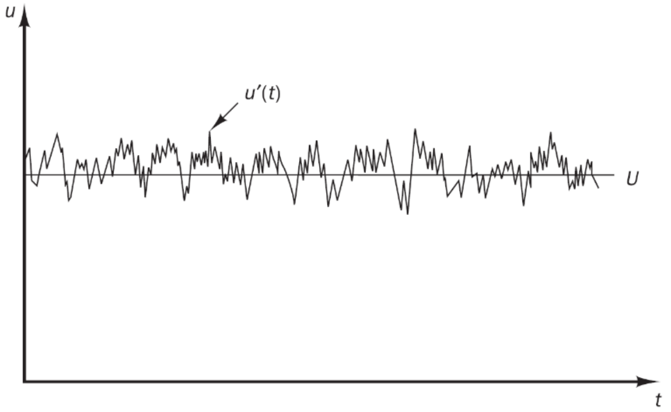

Figure 18 *Typical point velocity measurement in turbulent flow.*

The random nature of a turbulent flow does not allow to define the velocity variable in an easy way. For this reason, the velocity is decomposed into time-averaged component $\overline{U}$ and into a fluctuating component $u'(t)$. This is called the Reynolds decomposition (see Figure 18).

$$u(t) = \overline{U} + u'(t) \tag{16}$$

The mean velocity can be expressed as:

$$\overline{U} = \lim_{t\to\infty} \frac{1}{\Delta t} \int_0^{\Delta t} U(t)dt \tag{17}$$

This definition of the mean of a flow property is adequate for steady mean flows. In time-dependent flows the mean of a property at time t is taken to be the average of the instantaneous values of the property over many repeated identical experiments, the so-called 'ensemble average'.

The time average of fluctuations $u'(t)$ is, by definition, equal to zero:

$$\overline{u'} = \frac{1}{\Delta t} \int_{t_0}^{t_0+T} u'(t)dt \ \equiv 0 \tag{18}$$

The Reynold decomposition is applied also to the other time-dependent variables such as density, pressure, temperature etc.

The Navier-Stokes equation can be written as:

$$\begin{aligned} \frac{\partial U}{\partial t} + \mathrm{div}(\mathrm{U}\mathbf{u}) &= -\frac{1}{\rho}\frac{\partial \boldsymbol{P}}{\partial x} + \nu\, div\big(grad(U)\big) \\ &+ \frac{1}{\rho}\left[\frac{\partial(-\rho\overline{u'^2})}{\partial x} + \frac{\partial(-\rho\overline{u'v'})}{\partial y} + \frac{\partial(-\rho\overline{u'w'})}{\partial z}\right] \end{aligned} \tag{19}$$

$$\begin{aligned} \frac{\partial V}{\partial t} + \mathrm{div}(\mathrm{V}\mathbf{u}) &= -\frac{1}{\rho}\frac{\partial \boldsymbol{P}}{\partial y} + \nu\, div\big(grad(V)\big) \\ &+ \frac{1}{\rho}\left[\frac{\partial(-\rho\overline{u'v'})}{\partial x} + \frac{\partial(-\rho\overline{v'^2})}{\partial y} + \frac{\partial(-\rho\overline{v'w'})}{\partial z}\right] \end{aligned} \tag{20}$$

$$\begin{aligned} &\frac{\partial W}{\partial t} + \mathrm{div}(\mathrm{W}\mathbf{u}) \\ &= -\frac{1}{\rho}\frac{\partial \boldsymbol{P}}{\partial z} + \nu\, div\big(grad(W)\big) \\ &+ \frac{1}{\rho}\left[\frac{\partial(-\rho\overline{u'w'})}{\partial x} + \frac{\partial(-\rho\overline{v'w'})}{\partial y} + \frac{\partial(-\rho\overline{w'^2})}{\partial z}\right] \end{aligned} \tag{21}$$

Where $-\rho\overline{u'^2}$, $-\rho\overline{v'^2}$, $-\rho\overline{w'^2}$ are the three normal stresses, respectively τ_{xx}, τ_{yy} and τ_{zz}, and the terms $\tau_{xy} = \tau_{yx} = -\rho u'v'$, $\tau_{xz} = \tau_{zx} = -\rho\overline{u'w'}$, $\tau_{yz} = \tau_{zy} = -\rho\overline{v'w'}$ are the three shear stresses. All these stresses terms are called the Reynolds stresses.

5.4 Turbulent Flow Calculations

To describe a turbulent motion quantitatively, in addition to the intensity it is necessary to introduce the concept of spatial and time scales of turbulence. A typical characteristic of a turbulent flow is the presence of turbulent eddies of different length scale l_n, and some of them, with a characteristic size, contain most of the kinetic energy.

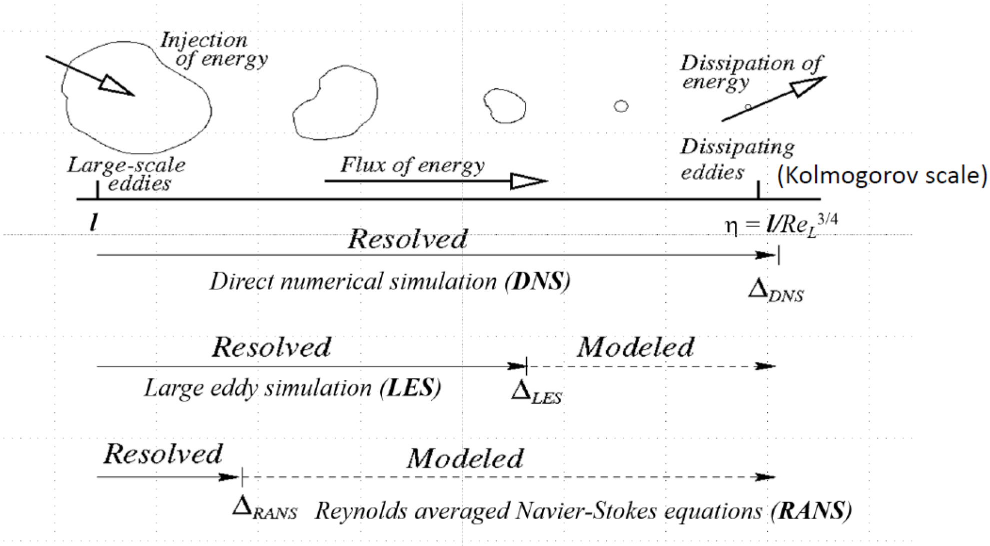

Figure 19 Basic approaches for the resolution of turbulence flows.

The system of governing equations of fluid flow, the Navier-Stokes equations, can be solved directly, without using any turbulence model this approach is called Direct Numerical Simulation (DNS). It can solve the unsteady Navier-Stokes equations on spatial grids that are so fine to resolve the Kolmogorov length scales at which energy dissipation takes place and with time steps small enough to resolve the period of the fastest fluctuations. Unfortunately, DNS approach requires very high costs in terms of computing resources, which make this approach impossible to be used for engineering applications and but only used for academic applications.

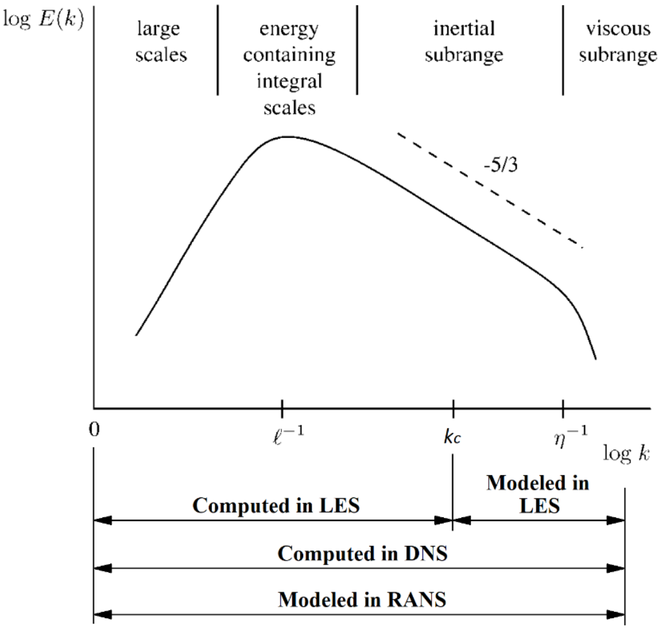

Figure 20 *Turbulent kinetic energy spectrum.*

To find a good compromise between computational cost and an accurate solution the use of a model is required. The two most common approaches are: Large Eddy Simulation (LES) and Reynolds averaged Navier-Stokes equations (RANS).

LES approach is an intermediate form of turbulence calculations which tracks the behaviour of the larger eddies. With this model the smaller eddies are filtered out and only the larger eddies are solved. The effects of the smallest, unresolved eddies, on the resolved flow, are included thanks to the so-called sub-grid scale model. Anyway, despite the reduction in computational time costs, the computing resources required are still too high.

The approach most widely spread in industrial applications is the RANS one, due to its modest computing resources required for reasonably accurate flow computations. This method focuses its attention on the mean flow and the effects of turbulence on mean flow properties. Before applying numerical methods, the Navier-Stokes equations are time-averaged and additional terms appear in time-averaged flow equations due to the interactions between various turbulent fluctuations. Extra terms are modelled via turbulence models such as $k-\varepsilon$ or Reynolds stress ones [1].

To be able to compute turbulent flows with the RANS equations it is necessary to develop turbulence models to predict the Reynolds stresses and the scalar transport terms. The most common RANS turbulence models are classified based on the number of additional transport equations that need to be solved with the RANS flow equations:

- Algebraic (Zero-Equation) models.
- One-Equations models, for example Spalart model. These RANS models are often used for easy numerical problems, because of their simplicity.
- Two-Equation models, which mainly are $k-\varepsilon$ model, $k-\omega$ model and their variations.
- Second-Order Closure models.

The $k-\varepsilon$ model is a more sophisticated and general, but also more expensive, description of turbulence which allows for the effects of transport of turbulence properties by convection and diffusion and for production and destruction of turbulence.

5.4.1 RNG $k-\varepsilon$ model

The modelled Reynolds stress for the RNG model is given by:

$$-\rho\overline{u_i'u_j'} = \mu_t\left(\frac{\partial\overline{u_i}}{\partial x_j}+\frac{\partial\overline{u_j}}{\partial x_i}\right)-\frac{2}{3}\rho\sigma_{ij}k \tag{22}$$

$$k=\frac{1}{2}\,\overline{u_i'u_j'}=\frac{1}{2}\left(\overline{u_x'u_x'}+\overline{u_y'u_y'}+\overline{u_z'u_z'}\right) \tag{23}$$

$$\mu_t=\rho C_\mu\sqrt{k}L=\rho\,C_\mu\frac{k^3}{\varepsilon} \tag{24}$$

Where σ_{ij} is the stress tensor, μ_t is the turbulent eddy viscosity, k is turbulent kinetic energy, C_μ is a constant that depends on the type of flow, L is the turbulence length scale and ε is the dissipation term of turbulent kinetic energy.

The turbulent diffusion and conductivity terms are:

$$D_t = \frac{\mu_t}{\rho Sc_t} \tag{25}$$

$$K_t = \frac{\mu_t}{\rho Pr_t}\, C_p \tag{26}$$

Where Sc_t is the turbulent Schmidt number and Pr_t is the turbulent Prandtl number.

To obtain the turbulent viscosity two equations are needed, one for the turbulent kinetic energy and one for the dissipation of turbulent kinetic energy.

The turbulent kinetic energy transport equation is given by:

$$\frac{\partial \rho k}{\partial t} + \frac{\partial \mathrm{\rho u_i k}}{\partial x_i} = \tau_{\mathrm{ij}} \frac{\partial u_i}{\partial x_j} + \frac{\partial}{\partial x_j} \frac{\mu + \mu_t}{Pr_k} \frac{\partial k}{\partial x_j} - \rho\varepsilon + \frac{C_s}{1.5} S_S \tag{27}$$

The transport equation for the dissipation of turbulent kinetic energy is given by:

$$\begin{aligned} \frac{\partial \rho\varepsilon}{\partial t} + \frac{\partial (\mathrm{\rho u_i \varepsilon})}{\partial x_i} &= \frac{\partial}{\partial x_j}\left(\frac{\mu + \mu_t}{Pr_\varepsilon} \frac{\partial \varepsilon}{\partial x_j}\right) + C_{\varepsilon_3}\, \rho\varepsilon \frac{\partial u_i}{\partial x_i} \\ &+ \left(C_{\varepsilon_1} \frac{\partial u_i}{\partial x_i}\, \tau_{ij} - C_{\varepsilon_2}\rho\varepsilon + C_S S_S\right) \frac{\varepsilon}{k} + S - \rho R_\varepsilon \end{aligned} \tag{28}$$

The last term of the equation, ρR_ε, defines the difference between standard k-ε and RNG k-ε models. If this term is present, the RNG k-ε model is used, otherwise is used the standard one. The RNG k-ε model can define different turbulence length scales, instead of considering only one, as in the standard model. This difference is fundamental to define all the contributions of the turbulence dissipation, being influenced by all the scales.

R_ε can be written as:

$$R_\varepsilon = \frac{\mathrm{C}_\mu \eta^3 \left(1 - \frac{\eta}{\eta_0}\right)}{1 + \beta\eta^3} \frac{\varepsilon^2}{k} \tag{29}$$

Where η and η_0 are:

$$\eta = \frac{k}{\varepsilon} \sqrt{2 S_{ij} S_{ij}} \tag{30}$$

$$\eta_0 = \left[\frac{\mathrm{C}_{\varepsilon 2} - 1}{\mathrm{C}_\mu (\mathrm{C}_{\varepsilon 1} - 1)}\right]^{0.5} \tag{31}$$

S_{ij} is the mean strain rate tensor and is defined as:

$$S_{ij} = \frac{1}{2}\left(\frac{\partial \overline{u_i}}{\partial x_j} + \frac{\partial \overline{u_j}}{\partial x_i}\right) \tag{32}$$

6. **CONVERGE**

In 1997 a group of graduate students, including Eric Pomraning, Keith Richards, Peter Kelly Senecal, Daniel Lee, and David Schmidt, founded Convergent Science, a computational fluid dynamic consulting company. Later Convergent Science became a computational fluid dynamics computer software company and in 2008 the first version of CONVERGE CFD software has been realised.

CONVERGE CFD software can simulate three-dimensional, reacting, or non-reacting, turbulent flows, including steady-state and transient simulations for incompressible or compressible flows.

The software contains a variety of physical models for phenomena such us turbulence, spray, conjugate heat transfer, multi-phase flow, fluid-structure interaction, and surface chemistry. For this reason, CONVERGE has been applied for modelling internal combustion engines, fuel injectors, gas turbines, pumps, compressors, and engine aftertreatment systems.

The strength of this software is the capability to create an autonomous mesh. CONVERGE features an automated meshing algorithm that generates an orthogonal mesh at runtime and applies the Adaptive Mesh Refinement (AMR) to refine the mesh during the simulation in areas with complex phenomena, like moving geometries or fluctuating temperatures or flow velocities.

6.1 Discretization Method

Discretization is the process of transferring continuous functions, models, variables, and equations into discrete counterparts.

There are different ways to approximate the flow variables: Finite Difference Method (FDM), Finite Element Method (FEM) and Finite Volume Method (FVM). Anyway, most of CFD codes are based on the last one, FVM.

6.2 Grid Control

On CONVERGE the base grid size (specified via dx_{base}, dy_{base}, and dz_{base}) can be controlled, before and during a simulation, by means of three tools: grid scaling, fixed embedding, and adaptive mesh refinement (AMR).

6.2.1 Grid Scaling

Grid scaling coarsens or refines the base grid size, CONVERGE uses the $grid_{scale}$ parameter to modify the base grid size according to:

$$scaled\ grid = \frac{dx_{base}}{2^{grid_{scale}}} \tag{33}$$

Where $grid_{scale}$ is the scaling factor (must be an integer) and $scaled\ grid$ is the new base grid size. A $grid_{scale}$ value of 0 leaves the base cells unchanged, a negative value coarsens the base grid, and a positive value refines the base grid. CONVERGE also scales dy_{base} and dz_{base} according to the previous equation

6.2.2 Fixed Embedding

The fixed embedding tool refines the grid at specific locations in the domain where a finer resolution is critical to the accuracy of the solution. For example, in a simulation of a sprays, an area of fixed embedding can be added by the nozzle to resolve the complex flow behaviour. The strong point of the fixed embedding tool is to finer only a limited area of the domain and leave the rest of the grid coarse, minimizing the simulation time.

The $embed\ scale$ parameter, which must be a positive integer, scales the base grid sizes according to:

$$dx_{embed} = \frac{dx_{base}}{2^{embed_{scale}}} \tag{34}$$

CONVERGE also scales dy_{base} and dz_{base} according to the previous equation .
To reduce the computational time, each fixed embedding can be activated starting for a specific time interval, refining the grid only for a portion of the simulation.
Different types of fixed embedding are supplied by CONVERGE:

- boundary embedding, which specifies the fixed embedding near the boundary selected,
- region embedding, which specifies the fixed embedding to the region selected,
- sphere embedding, which specifies the fixed embedding to a spherical area defined by a centre and a radius,
- cylinder embedding, which specifies the fixed embedding to a cylindrical area defined by a centre and a radius for both bases,
- box embedding, which specifies the fixed embedding to a cubic area defined by a centre and half-length of each dimension of the box,
- nozzle and injector embedding, which specifies a conical area of fixed embedding around the nozzle selected.

6.2.3 Adaptive Mesh Refinement (AMR)

The Adaptive Mesh Refinement (AMR) tool automatically refines the grid based on fluctuating and moving conditions such as temperature or velocity.

Especially during the simulation of complex phenomena, such as flame propagation or high-velocity flow, AMR can be a relevant factor to save time resolution, adding higher grid resolution where the flow field is most under-resolved or where the gradient of a specific field variable is the highest. The efficiency of AMR depends on the accuracy of the algorithm used.

6.3 Volume of Fraction (VOF) Modelling

A way to simulate multi-phase flows is to use the volume of fluid (VOF) method, which is a Eulerian method that locates and tracks the free surface in a liquid-gas flow or the interface in a liquid-liquid flow. It can be used with both compressible and incompressible fluids.

As suggested by the name, the VOF method tracks the volume of fluid within each cell and represents it by the void fraction variable α, which is the fraction of the cell's volume that does not contain fluid (see Figure 21):

- $\alpha = 0$ the cell contains only liquid.
- $0 < \alpha < 1$ the cell contains both liquid and gas.
- $\alpha = 1$ the cell contains only gas.

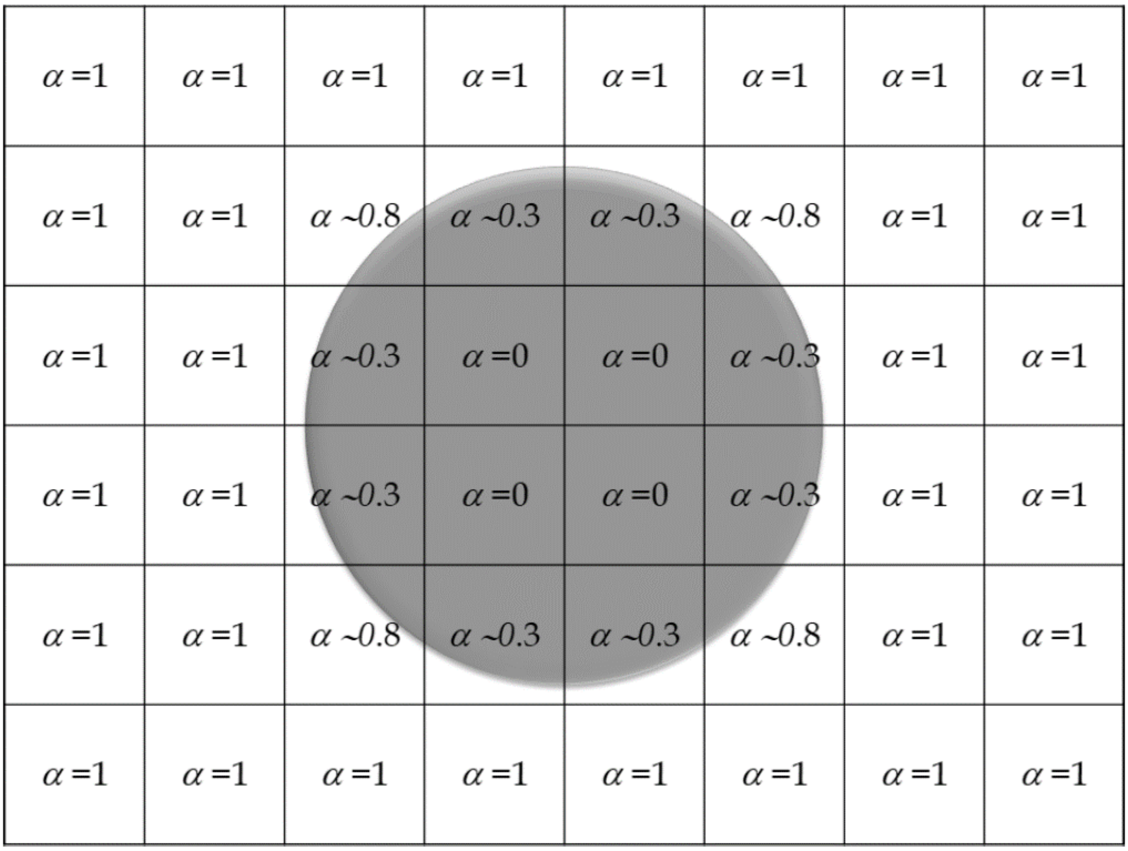

α =1	α =1	α =1	α =1	α =1	α =1	α =1	α =1
α =1	α =1	α ~0.8	α ~0.3	α ~0.3	α ~0.8	α =1	α =1
α =1	α =1	α ~0.3	α =0	α =0	α ~0.3	α =1	α =1
α =1	α =1	α ~0.3	α =0	α =0	α ~0.3	α =1	α =1
α =1	α =1	α ~0.8	α ~0.3	α ~0.3	α ~0.8	α =1	α =1
α =1	α =1	α =1	α =1	α =1	α =1	α =1	α =1

Figure 21 *Void fraction* $\boldsymbol{\alpha}$ *values. The grey circle represents a liquid droplet.*

It is important to specify that the void of fraction variable does not contain any information about the shape or the location of any interface within the cell. Anyway, two interface reconstruction methods are available in CONVERGE: the Piecewise-Linear Interface Calculation (PLIC) method and the High-Resolution Interface Capturing (HRIC) scheme. The first method constructs a fluid interface from a local planar interface within each cell, the second one constructs an interpolated curved interface using information from neighbouring cells. HRIC is more stable than PLIC, but it is more computationally expensive, and it cannot resolve an interface as sharply.

Basically, the void fraction α is solved by the following conservation equation:

$$\frac{\partial \alpha}{\partial t} + \frac{\partial}{\partial x_i}(u_i \alpha) = 0 \tag{35}$$

And the global density is solved as:

$$\rho = \alpha \rho_g + (1 - \alpha)\rho_l \tag{36}$$

Where ρ_g is the gas density and ρ_l is the liquid density in the cell.

6.4 SPRAY MODELS

Several spray breakup mechanisms are available on CONVERGE, such as the Kelvin-Helmholtz (KH) and Rayleigh-Taylor instability mechanisms, LISA sheet breakup model, Taylor Analogy Breakup (TAB) drop breakup model and Eulerian-Lagrangian Spray Atomization (ELSA) model for the prediction of primary spray breakup.

- Kelvin-Helmholtz Breakup Model

  The Kelvin–Helmholtz instability typically occurs when there is velocity a shear in a single continuous fluid, in different words where there is a velocity difference across the interface between two fluids.

On CONVERGE, a variation of the original KH model, called KH-ACT Model, is present. It differs from the original because it also includes the effects of aerodynamics, cavitation, and turbulence on primary breakup.

- Rayleigh-Taylor Breakup Model
  The Rayleigh–Taylor instability is an instability of an interface between two fluids of different densities which occurs when the lighter fluid is pushing the heavier fluid.
- KH-RT Breakup Length Model
  CONVERGE allows the user to combine the RT and KH model together. If the KH-RT Breakup Length Model is used an intact core of breakup length can be find out as:

$$L_b = C_{bl}\sqrt{\frac{\rho_l}{\rho_g}}\,d_0 \tag{37}$$

Where C_{bl} is the breakup length constant and d_0 is the diameter of the blob injected with the same diameter of the injector nozzle.

This combined model assumes that only KH instabilities are responsible for drop breakup inside of the characteristic breakup distance L_b, while both KH and RT mechanisms are active for distances larger than L_b (see Figure 22).

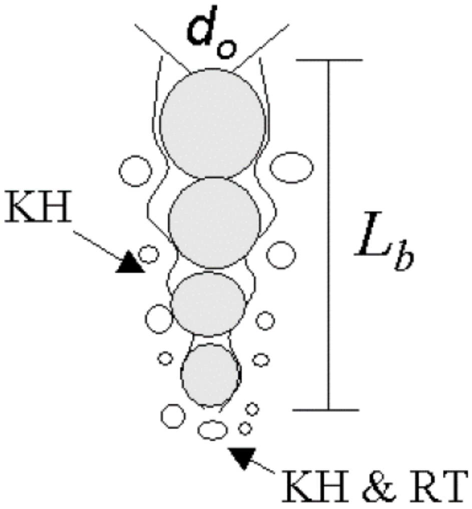

Figure 22 *Schematic of the KH-RT spray.*

6.5 VOF-Spray One-Way Coupling

On CONVERGE it is possible to simulate a spray combining the VOF method with the Lagrangian one, this method is called *VOF-Spray One-Way Coupling*. The advantage to use this method is to combine a high-fidelity simulation of a fuel injector and nozzle (VOF) with a low-cost parcel-based fuel injector spray simulation (Lagrangian).

At first, a VOF simulation is run, in this phase is important to define the domain upstream the orifice outlet and identify the injectors and nozzles. As results of this simulation an outlet file, with the name of *vof_spray.out,* is generated. This file contains parcel position, velocity, turbulence, temperature, and cell size information, particularly these data are referred to two layers of cells on either side of a region interface that defines the nozzle.

After that, it is needed to run a Lagrangian simulation, where the outlet file, *vof_spray.out*, generated in the previous step, becomes an input file with the name *vof_spray.dat.* In this phase it is important to define the domain downstream to the orifice outlet so that the simulation uses the data and injector settings (position, orientation, and diameter) in *vof_spray.dat* to create parcels and represent the spray.

On CONVERGE one example of how the VOF-Spray One-Way Coupling method works is shown in the example case SPRAY G.

7. **Experiment**

To create a CFD model, capable of reproducing the atomization of FPBO, an experimental work, as starting point, was fundamental. In literature a lot of studies on the atomization of this bio-oil have been published, but one of the purposes of this thesis is to obtain a good atomization for future applications with gas turbines. So that, one of the aspects considered during the review of the experimental works was that the SMD should have been around 50micros. Another aspect considered was that the fuel sprayed should have been 100% PO and, preferable, not a blend.

Therefore, the experimental work, which have been considered better fitting to the purpose of this thesis, is the one published in 2019 by Sangsig Yun, Minji Choi, and Ashwani Kumar in Ottawa [12].

The subject of this research work was to evaluate the spray performance of FPBO, and to better understand the atomization of FPBO different tests have been done. Two types of nozzles have been used, at first a pressure atomizer and secondly an air blast one. In addition, pyrolysis oils from different suppliers, whose physical properties were slightly different, have been used. From these tests was possible to understand how the impact of the atomizer design and the physical properties affect the spray performance.

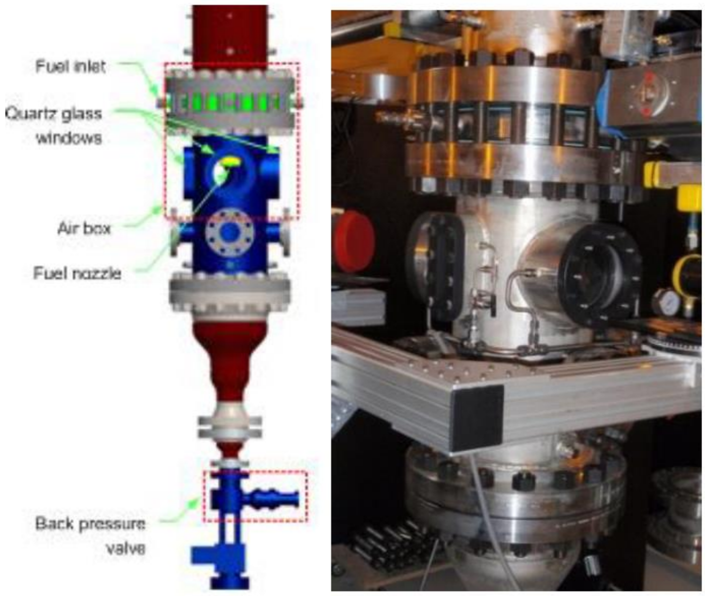

Figure 23 *Test facility for the investigation of atomization of FPBO*

The test facility, used in this experimental work, is shown in the **Figure 23**, the nozzle is located into the air box and thanks to the quartz glass windows was possible to observe and measure the droplet size distribution, the penetration depth, and the cone angles.

The most important component of the test facility is the laser diagnostic equipment, in this work were included the Malvern laser diffraction particle laser and the long-distance microscopic image technique (shadowgraph). To be more precise the Malvern was used to measure the main droplet, due to its capability of taking rapid measurements, and the shadowgraph was used as the main visual measurement method for a preliminary analysis.

The five samples of bio-oil were selected from different suppliers, as consequence the physical properties were not the same. In the **Table 3** are reported the C, H and N mass fractions, the densities at 20°C, the HHV values and finally the viscosities at different temperatures for each sample.

Sample	Ext-A	CE-HWS-1	CE-HWS-2	Ext-A	CE-HWS-3
C %wt	41.1%	49.9%	46.5%	43.2%	42.6%
H %wt	7.78%	8.44%	8.20%	7.52%	7.70%
N %wt	0.16%	<0.15%	<0.15%	<0.15%	<0.15%
Density at 20°C [kg/m^3]	1217	1215	1224	1211	1184
HHV [MJ/kg]	16.4	18.1	17.9	17.5	18.5
Viscosity at 20°C [cSt]	227.2	212.6	173.2	94.85	34.16
Viscosity at 40°C [cSt]	65.10	70.32	50.00	34.83	14.21
Viscosity at 60°C [cSt]	14.70	18.60	13.20	12.32	6.07

Table 3 *Sample physical properties*

In the first part of the project, it has been studied the atomization with a common pressure swirl atomizer. Due to the limited quantity of FPBO samples, for this test it has been used only the sample CE-HWS-2. The results were not good, confirming that this nozzle configuration is not adapt for a bio-oil with the physical properties of FPBO.

Successively, the tests have been performed using a commercially available air-blast nozzle (Delavan, P/N 30609). Since the results were much better than the one obtained with the pressure atomizer, in this phase it was possible to evaluate its characteristics for wide range of atomizing air flow rates, fuel temperature and different samples.

The spray conditions for the testes with air-blast nozzle are summarise in the Table 4:

Sample	Pyrolysis oils Ext. A, Ext. B, CE-HWS-1, CE-HWS-3
Fuel Temperature	25 - 60˚C
Fuel flow rate	0.5 - 0.76 g/s
Atomization air flow rate	5 - 15 LPM

***Table 4** Spray test conditions for air assist atomizer*

The shadowgraph imaging technique shows that in the zone close to the outlet of the long and thick fuel ligaments are formed and any immediate break-up processes into small droplets are not observed due to high viscosity of fuel, which leads to poor atomization. However, more significant improvement of the atomization process was achieved by increasing the atomization air flow rate as show in the **Figure 24**.

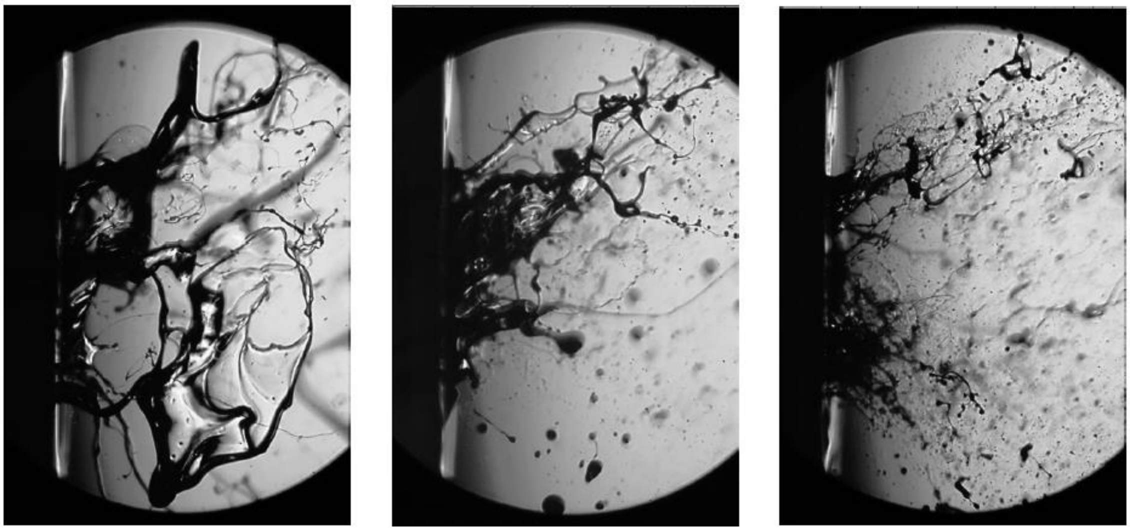

***Figure 24** Fuel temperature 20°C, atomization air 10LPM (left) - Fuel temperature 60°C, atomization air 10LPM (middle) - Fuel temperature 60°C, atomization air 15LPM (right)*

The droplet sizes (SMD) of the fuel spray were measured using Malvern laser diffraction particle sizer and the results are shown in the **Figure 25**.

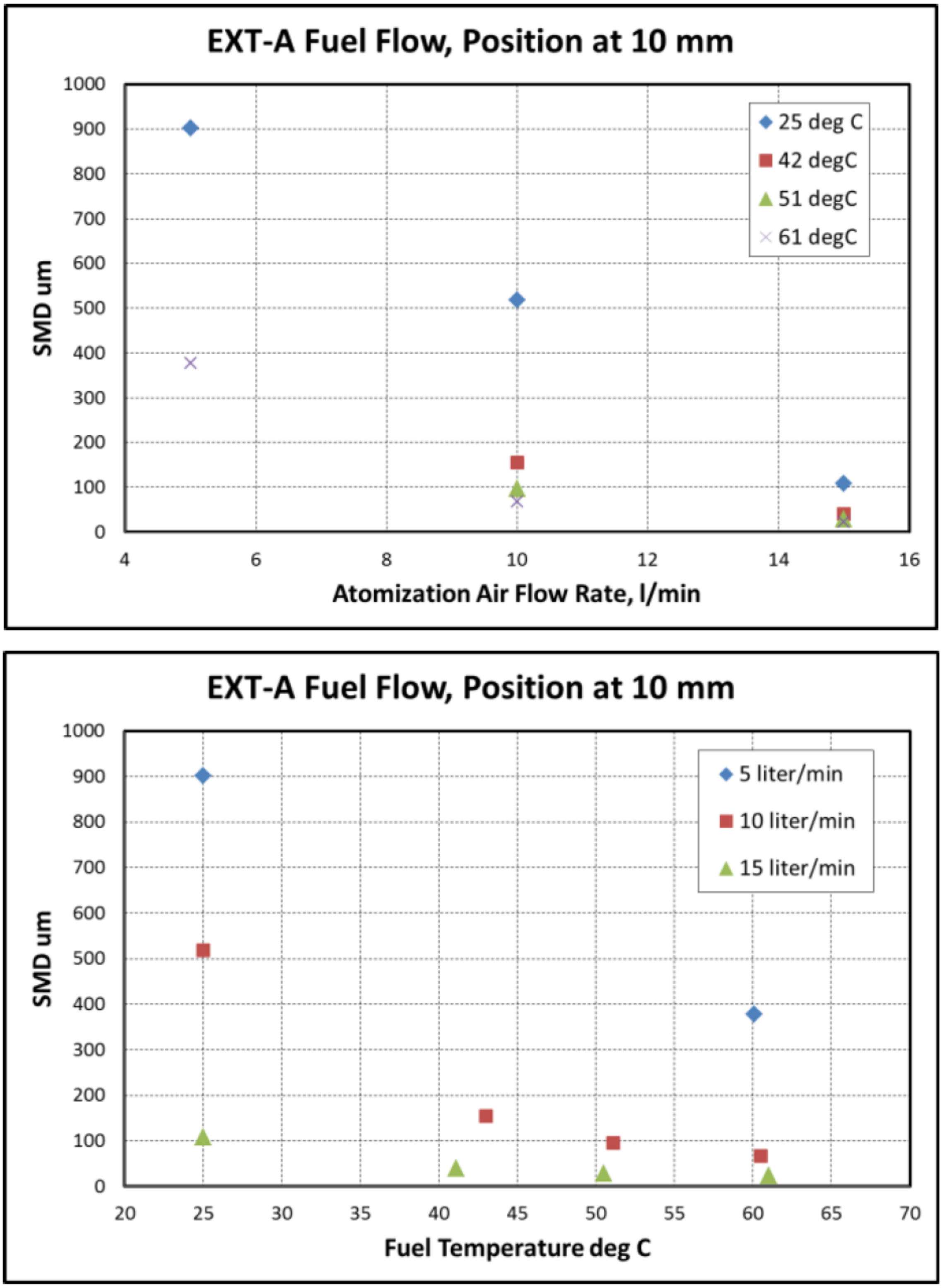

Figure 25 *Sauter mean diameter (SMD) vs atomization air (top) - Sauter mean diameter (SMD) vs fuel temperature (bottom)*

As expected, increasing the air flow rate the relative velocity between the air flow and the fuel increases, performing a better atomization. And, obviously, increasing the fuel temperature, its viscosity decreases and so the SMD of the spray is smaller.

An SMD of 50 micros has been obtain with the following conditions:

Sample	Ext. A
Fuel Temperature	60˚C
Fuel flow rate	0.76 g/s
Atomization air flow rate	15 LPM

Table 5 *Spray test conditions for air assist atomizer (SMD = 50microns)*

8. Surrogate characterization

For experimental research and numerical modelling, complex fuels need to be defined by a surrogate, which is a mixture of one or more simple compounds (or fuels) that can emulate the physical properties or combustion properties of the original fuel.

FPBO is a complex fuel whose chemical composition is not known completely, for this reason its characterization by a surrogate is a challenging task. It is important to highlight that a surrogate mixture designed for one specific purpose is not certain that it is appropriate for another specific purpose. For example, physical properties such as conductivity, density, viscosity, volatility are fundamental to describe the fuel atomization and evaporation, while the chemical composition influences the combustion properties such as the pollution formation or the flame speed.

Compound		Chemical formula	%y_i
1	Levoglucosan	C6H10O5	29.64
2	Water	H2O	22.00
3	Vanillin	C8H8O3	17.94
4	Alkali Lignin	C20H26O8	7.80
5	Ethylene Glycol	C2H6O2	5.46
6	Glycol Aldehyde	C2H4O2	5.46
7	2,5 Dimethylfuran	C6H8O	5.46
8	Acetic Acid	CH3COOH	3.90
9	Oleic acid	C18H34O2	2.34

Table 6 *FPBO Surrogate composition by A. Frassoldati et al.* [16]**.**

A relevant contribution in the definition of a surrogate for FPBO comes from A. Frassoldati and his colleagues [15]. The surrogate proposed by A. Frassoldati et al., in 2007 and still object of study, is reported in the **Table 6**. The compounds reported in the table have been selected from a wide list of species previously proposed to describe the different chemical functionalities of FPBO, considering safety issued, availability and the handling of these species.

Generally, to characterize a fluid is fundamental to know how the physical properties of each compound vary with temperature. After that, for each component and for each property, it is possible to find out the coefficients of a temperature dependent regression equation, which simulates the behaviour of the corresponding compound for the corresponding physical property.

For the most common components it is not needed to compute these coefficients by hand because they are already reported in specific handbooks, one of the widespread, for example, is **CARL L. YAWS. (2015). THERMOPHYSICAL PROPERTIES OF CHEMICALS AND HYDROCARBONS** [17].

	Compound	**T_c [K]**	**P_c [bar]**	**V_c [ml/mol]**	**ρ_c [kg/m^3]**	**ω [-]**
1	Levoglucosan	791.00	56.90	370.0	0.4535	1.437
2	Water	647.13	22.06	56.0	0.322	0.345
3	Vanillin	777.00	40.10	415.0	0.3666	0.757
4	Alkali Lignin	[-]	[-]	[-]	[-]	[-]
5	Ethylene Glycol	720.00	82.00	170.6	0.3638	0.507
6	Glycol Aldehyde	586.22	63.29	171.4	0.3503	0.768
7	2,5 Dimethylfuran	557.13	41.73	306.5	0.3136	0.332
8	Acetic Acid	591.95	57.86	179.7	0.3342	0.467
9	Oleic acid	781.00	13.90	1000.0	0.2825	1.182

Table 7 *Critical properties of the compounds which are composing the FPBO surrogate.*

The critical properties of the species composing the surrogate mixture collected by A. Frassoldati et al are reported in the **Table 7**. T_c is the critical temperature, P_c the critical pressure, V_c the critical volume, ρ_c the critical density and ω the acentric factor.

These properties were taken from Yaws' database[17] or estimate through Joback method[18].

8.1 Density

The regression equation for the density is:

$$\rho = A\,B^{-\left(1-\frac{T}{C}\right)^{n}} \tag{38}$$

Where ρ is the saturated liquid density [g/ml] and *A, B, C, n* are the regression coefficients. In **Table 8** the range of validity is specified.

	Compound	A	B	C	n	T_{min} [K]	T_{max} [K]
1	Levoglucosan	0.4535	0.23377	791.00	0.33009	456.00	791.00
2	Water	0.3471	0.274	647.13	0.28571	273.16	647.13
3	Vanillin	0.36660	0.29674	777.00	0.28571	355.00	777.00
4	Alkali Lignin	[-]	[-]	[-]	[-]	[-]	[-]
5	Ethylene Glycol	0.3638	0.29432	720.00	0.17200	260.15	720.00
6	Glycol Aldehyde	0.3503	0.26987	592.71	0.22547	222.71	592.71
7	2,5 Dimethylfuran	0.31363	0.27562	557.13	0.28571	210.35	557.13
8	Acetic Acid	0.3520	0.26895	592.71	0.26843	289.81	592.71
9	Oleic acid	0.26020	0.25366	936.00	0.28970	286.53	936.00

Table 8 *Regression coefficients for the evaluation of density.*

The density of the mixture can be approximated as:

$$\rho_m = \frac{1}{\sum_i \frac{y_i}{\rho_i}} \tag{39}$$

Where y_i is the mass fraction of the *i*-th species and ρ_i is the density of the *i*-th pure species. To validate the surrogate properties, these have been compared, when possible, with data present in literature.

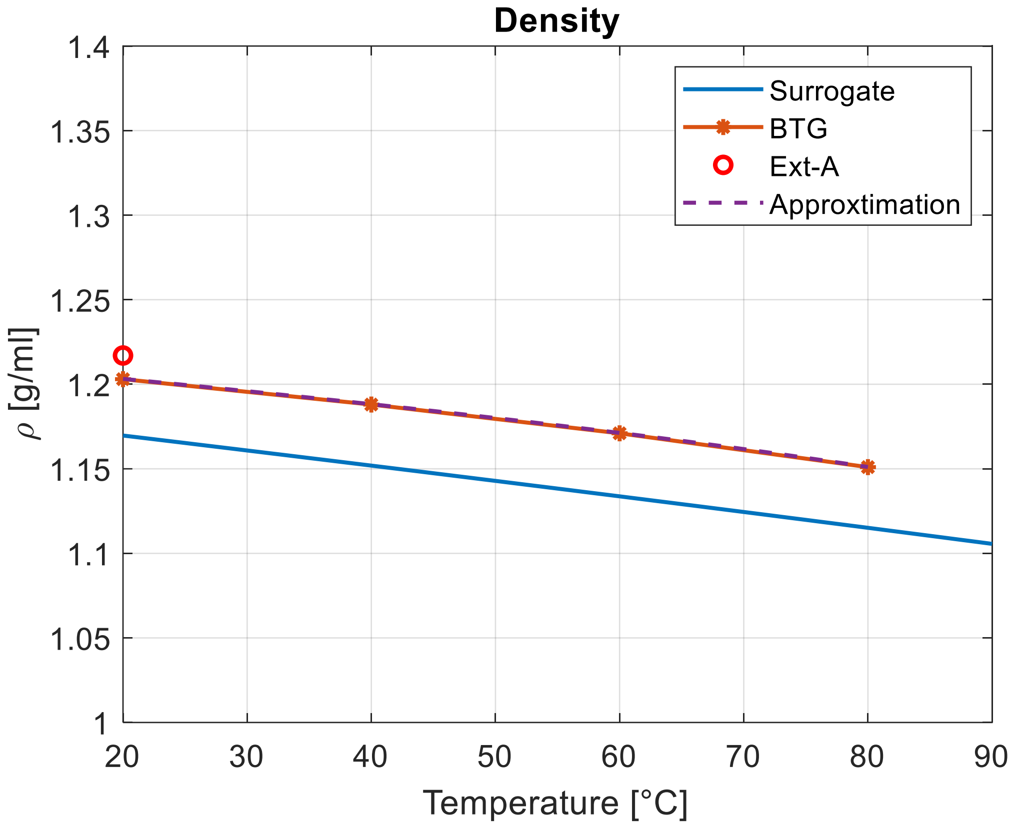

Figure 26 *Density comparison.*

In **Figure 26** the blue line is the density obtained by mixing the surrogate components, except for Alkali Lignin whose data are not available. The orange line represents the density of the BTG oil measured by VTT [19]. BTG oil is a variety of FPBO obtained from pines and already commercially available. Note that, some physical properties of BTG oil are similar to the one of the fuel sample (Ext-A) used in the experiment of S.Yun. The red dot is the value of density at 20°C of the sample Ext-A.

As can easily notice in the **Figure 26** the BTG density is closer to the one of the fuel sample Ext-A, and so, for a better simulation, it has been assumed that each component has the same density, in a temperature range from 20 to 80°C, of BTG oil. Consequently, can be defined a unique regression equation, valid for the surrogate mixture. This new equation is represented by a purple dot line in the **Figure 26**, and the corresponding coefficients are:

Compound	A	B	C	n
Surrogate mixture	1.0501	0.7810	394.5436	0.4393

8.2 Viscosity

The regression equation for the viscosity is:

$$\log_{10} \eta = A + \frac{B}{T} + C\,T + D\,T^2 \tag{40}$$

Where η is the liquid viscosity [cp] and *A, B, C, D* are the regression coefficients. In the **Table 9** the range of validity is specified.

Compound		A	B	C	n	T_{min} [K]	T_{max} [K]
1	Levoglucosan	[-]	[-]	[-]	[-]	[-]	[-]
2	Water	-10.216	1.79E+03	1.77E-02	-1.26E-05	273	643
3	Vanillin	-17.2771	3.4485E+03	2.9612E-02	-1.8943E-05	445	715
4	Alkali Lignin	[-]	[-]	[-]	[-]	[-]	[-]
5	Ethylene Glycol	-16.5536	3.1616E+03	3.0715E-02	-2.2078E-05	400	600
6	Glycol Aldehyde	[-]	[-]	[-]	[-]	[-]	[-]
7	2,5 Dimethylfuran	-8.5394	1.1507E+03	2.1154E-02	-2.1514E-05	300	506
8	Acetic Acid	-3.8937	7.8482E+02	6.6650E-03	-7.5606E-06	290	593
9	Oleic acid	-6.1303	1.6893E+03	8.3740E-03	-6.4505E-06	400	781

Table 9 Regression coefficients for the evaluation of viscosity.

The viscosity of the mixture can be approximated as:

$$ln\, \eta_m = \sum_i x_i \; ln\, \eta_i \qquad (41)$$

Where x_i is the mole fraction of the *i*-th species and η_i is the viscosity of the *i*-th pure species.

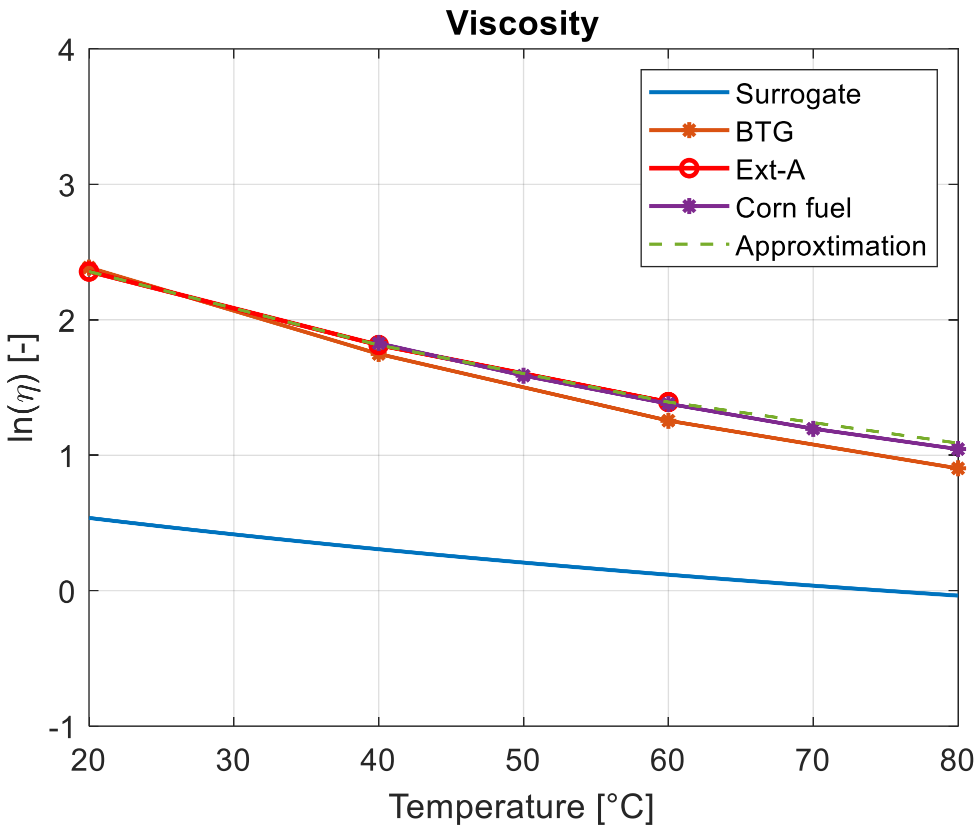

Figure 27 *Viscosity comparison.*

In the **Figure 27** the blue line is the viscosity obtained by mixing the surrogate components, except for the species whose data were not available. The orange line represents the viscosity of the BTG oil measured by VTT [19]. The purple line represents the viscosity of Corn fuel oil produced by Biomass Technology Group and used in several studies on FPBO properties, due to their similarity [20]. Finally, the red line is referred to the viscosity of the sample Ext-A.

As shown in the **Figure 27** the Corn fuel viscosity trend is closer to the one of the sample Ext-A used, and so, for a better imitation, it has been assumed that each component has the same coefficients of the viscosity regression equation. So, the viscosity follows the trend of the fuel sample Ext-A, in the temperature range of 20-60°C, and the one of Corn fuel oil from 60°C to 80°C (see the green dot line).

The coefficients of this new regression equation are:

Compound	A	B	C	n
Surrogate mixture	14.70	1.00	-0.0888	0.0001197

8.3 Surface tension

The regression equation for the surface tension is:

$$\sigma_i = A\left(1 - \frac{T}{T_c}\right)^n \tag{42}$$

Where σ_i is surface tension [dynes/cm] and *A,* T_c*, n* are the regression coefficients. In **Table 10** the range of validity is specified.

Compound		A	T_c	n	T_{min} [K]	T_{max} [K]
1	Levoglucosan	[-]	[-]	[-]	[-]	[-]
2	Water	132.67	647.13	0.955	273.16	647.13
3	Vanillin	92,62	777.00	1.336	355.00	777
4	Alkali Lignin	[-]	[-]	[-]	[-]	[-]
5	Ethylene Glycol	106.49	645.00	1.222	260.15	645.00
6	Glycol Aldehyde	[-]	[-]	[-]	[-]	[-]
7	2,5 Dimethylfuran	63.81	550.13	1.222	210.35	550.13
8	Acetic Acid	57.05	592.71	1.070	289.81	592.71
9	Oleic acid	53.29	781.00	1.039	286.53	633.15

Table 10 *Regression coefficients for the evaluation of surface tension.*

The surface tension of the mixture can be approximated as:

$$\sigma_m = \sum_i x_i \sigma_i \tag{43}$$

Where x_i is the mole fraction of the *i*-th species and σ_i is the surface tension of the *i*-th pure species, except for the compounds whose data were not available.

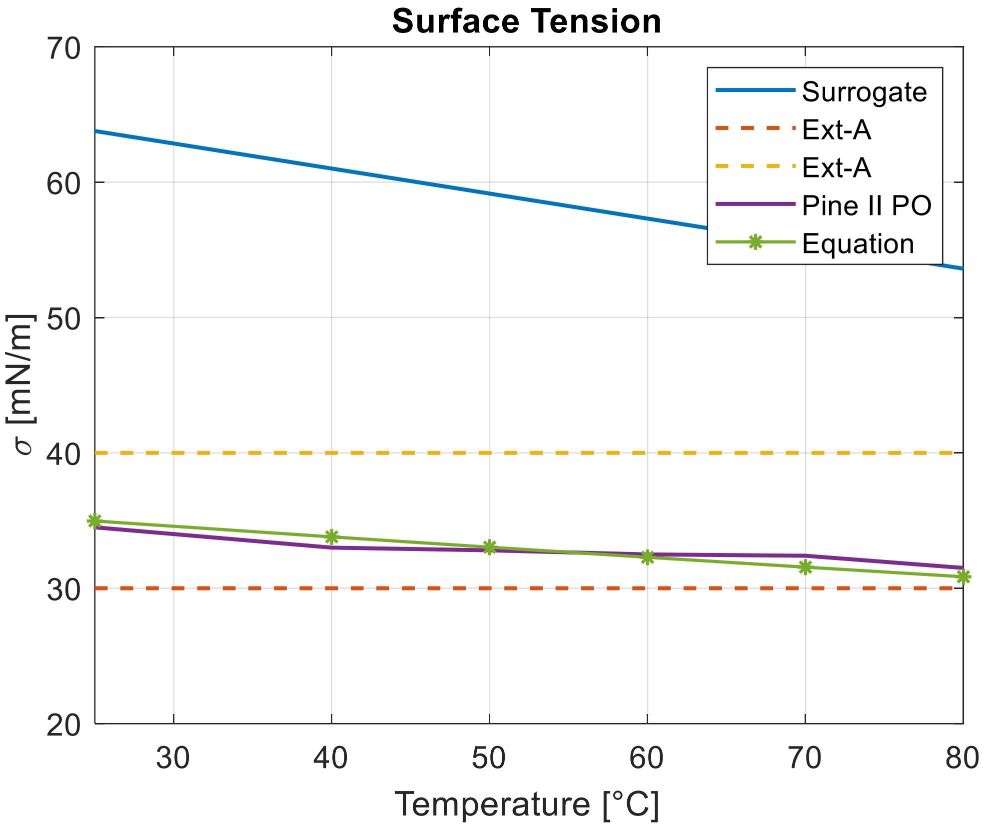

Figure 28 *Surface tension comparison.*

In the **Figure 28** the blue line is the surface tension obtained by mixing the surrogate species. The dot lines delimit a surface tension range into which the one of the sample Ext-A is included. Then, the purple line indicates the surface tension of a pyrolysis oil obtained from Pines [20].

The surrogate is overestimating the surface tension of the sample, for this reason it has been assumed that all the species composing the surrogate have the same surface tension trend and so the same coefficients of the regression equation for the surface tension.

Compound	**A**	**T_c**	**n**
Surrogate mixture	69.032	26013882.22	59335.042

8.4 Heat Capacity

The regression equation for the heat capacity is:

$$C_p = A + B\,T + C\,T^2 + D\,T^3 \tag{44}$$

Where C_p is the heat capacity [J/mol/K] and *A, B, C, D* are the regression coefficients. In the **Table 11** the range of validity is specified.

	Compound	**A**	**B**	**C**	**n**	**T_{min} [K]**	**T_{max} [K]**
1	Levoglucosan	337.4	Sallevelt et al. [5]				
2	Water	92.053	-4.00E-02	-2.11E-04	5.35E-07	273	615
3	Vanillin	-8.950	1.7876	-3.6684E-03	2.9525E-06	356	699
4	Alkali Lignin	[-]	[-]	[-]	[-]	[-]	[-]
5	Ethylene Glycol	75.878	6.4182E-01	-1.6493E-03	1.6937E-06	261	581
6	Glycol Aldehyde	[-]	[-]	[-]	[-]	[-]	[-]
7	2,5 Dimethylfuran	25.453	1.2507	-4.3416E-03	5.9138E-06	293	323
8	Acetic Acid	-18.8944	1.0971	-2.8921E-03	2.9275E-06	291	533
9	Oleic acid	278.686	2.5434	-5.4355E-03	4.9240E-06	288	703

Table 11 *Regression coefficients for the evaluation of heat capacity.*

The heat capacity of the mixture can be approximated as:

$$C_{p_m} = \sum_i x_i C_{p_i} \tag{45}$$

Where x_i is the mole fraction of the *i*-th species and C_{p_i} is the heat capacity of the *i*-th pure species.

In the **Figure 29** the blue line is the heat capacity obtained by mixing the surrogate components, except for Alkali Lignin whose data are not available. The orange dot line represents the average value of heat capacity of FPBO estimated by Peacocke et al. in 1994 and the yellow one the average value estimated by Qiang et al in 2008 [6].

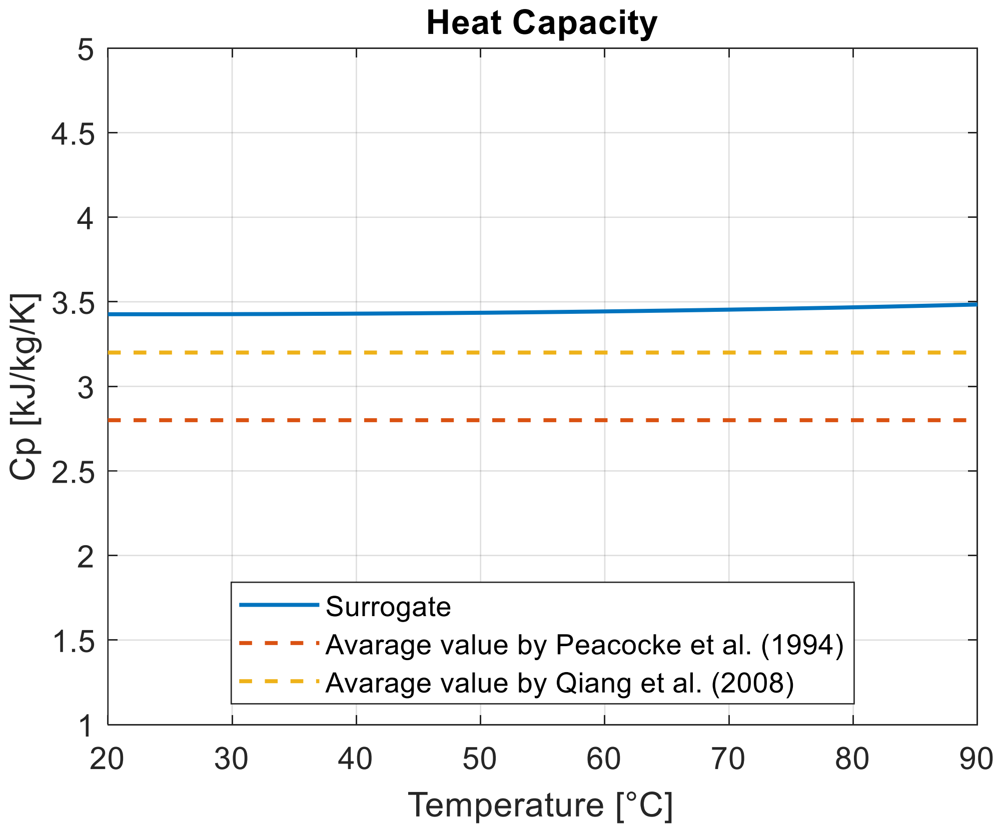

Figure 29 *Heat Capacity comparison.*

By comparing the heat capacity trend of the surrogate and the average values reported in literature, the surrogate is slightly overestimating the average values, so it can be considered acceptable.

8.5 Thermal Conductivity

The regression equations for the thermal conductivity are:

$$log_{10} k_{liq} = A + B\left(1 - \frac{T}{T_c}\right)^{\frac{2}{7}} \tag{46}$$

$$k_{H_2O} = A + BT + CT^2 \tag{47}$$

Where k_{liq} is the liquid thermal conductivity [W/m/K] and *A, B,* T_c and *C* are the regression coefficients. Note that organic and inorganic, such as water, species have a different regression equation. In the **Table 12** the range of validity is specified.

	Compound	A	B	T_c / C	T_{min} [K]	T_{max} [K]
1	Levoglucosan	[-]	[-]	[-]	[-]	[-]
2	Water	-0.2758	4.61E-03	-5.54E-06	273	633
3	Vanillin	-1.7080	1.0230	777.00	355	738
4	Alkali Lignin	[-]	[-]	[-]	[-]	[-]
5	Ethylene Glycol	-0.5918	-	645.00	260	613
6	Glycol Aldehyde	[-]	[-]	[-]	[-]	[-]
7	2,5 Dimethylfuran	-2.3713	1.7446	720.00	267	422
8	Acetic Acid	-1.2836	0.5893	592.71	290	563
9	Oleic acid	-2.9905	2.6266	781.00	287	742

***Table 12** Regression coefficients for the evaluation of thermal conductivity.*

The thermal conductivity of the mixture can be approximated as:

$$k_m = \left(\sum_i y_i k_i^{-2}\right)^{-0,5} \tag{48}$$

Where x_i is the mole fraction of the *i*-th species and k_i is the thermal conductivity of the *i*-th pure species.

In **Figure 30** is shown the blue line, which is the thermal conductivity obtained by mixing the surrogate components, except for those species whose data were not available. In the graph it is present also the average value proposed by Peacocke in 1994 [6], represented by the orange dot line. In this case the surrogate is widely underestimating the thermal conductivity of FPBO. So, it has been assumed that all the compounds of the surrogate have the same thermal conductivity, that is assumed to be constant and equally to the average value measured by Peacocke.

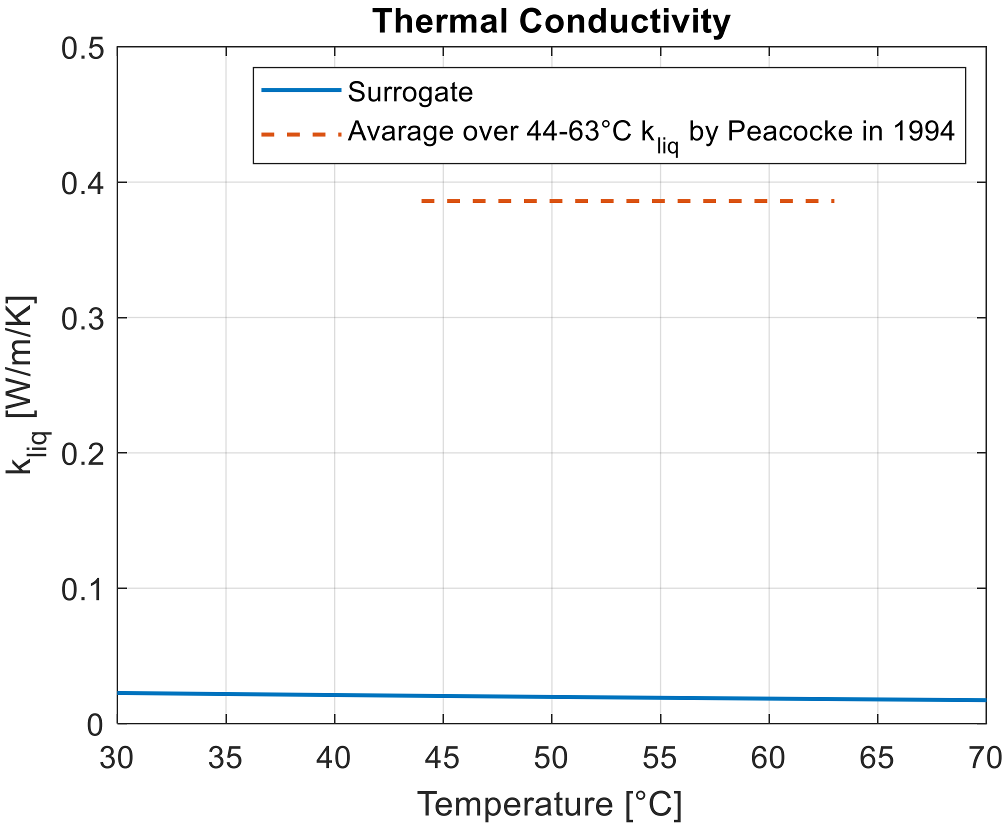

Figure 30 *Thermal conductivity comparison.*

8.6 Vapour Pressure and Enthalpy of Vaporisation

The regression equation for the vapour pressure is:

$$\log_{10} P = A + \frac{B}{T} + C\ \log_{10} T + D\,T + E\,T^2 \tag{49}$$

Where P is the vapour pressure [mmHg] and *A, B, C, D, E* are the regression coefficients. In the **Table 13** the range of validity is specified.

Compound		A	B	C	D	E	T_{min} [K]	T_{max} [K]
1	Levoglucosan	$\ln(P[Pa]) = 40.99 - \frac{15824}{T[K]}$ [21]						
2	Water	29,8605	-3,15E+03	-7,30E+00	2,42E-09	1,81E-06		
3	Vanillin	-25.5830	-4.1E+03	1.8E+01	-2.8E-02	1.1E-05	355	777
4	Alkali Lignin	[-]	[-]	[-]	[-]	[-]	[-]	[-]
5	Ethylene Glycol	82.4062	-6.3E+03	-2.5E+01	-2.4E-09	8.7E-06	260.15	645
6	Glycol Aldehyde	$\log10(P[Pa]) = 12.96 - \frac{3657}{T[K]}$ [22]						
7	2,5 Dimethylfuran	29.9561	-3.0E+03	-6.8E+00	-7.8E-03	1.0E-05	270.42	390.48
8	Acetic Acid	28.3756	-3.0E+03	-7.0E+00	-1.5E-09	2.2E-06	289.81	592.71
9	Oleic acid	78.6973	-8.8E+03	-2.2E+01	4.8E-11	2.7E-06	286.53	633.15

Table 13 *Regression coefficients for the evaluation of vapour pressure.*

The vapour pressure of the mixture can be approximated as:

$$P_m = \sum_i x_i \, P_i \tag{50}$$

Where x_i is the mole fraction of the *i*-th species and P_i is the vapour pressure of the *i*-th pure species.

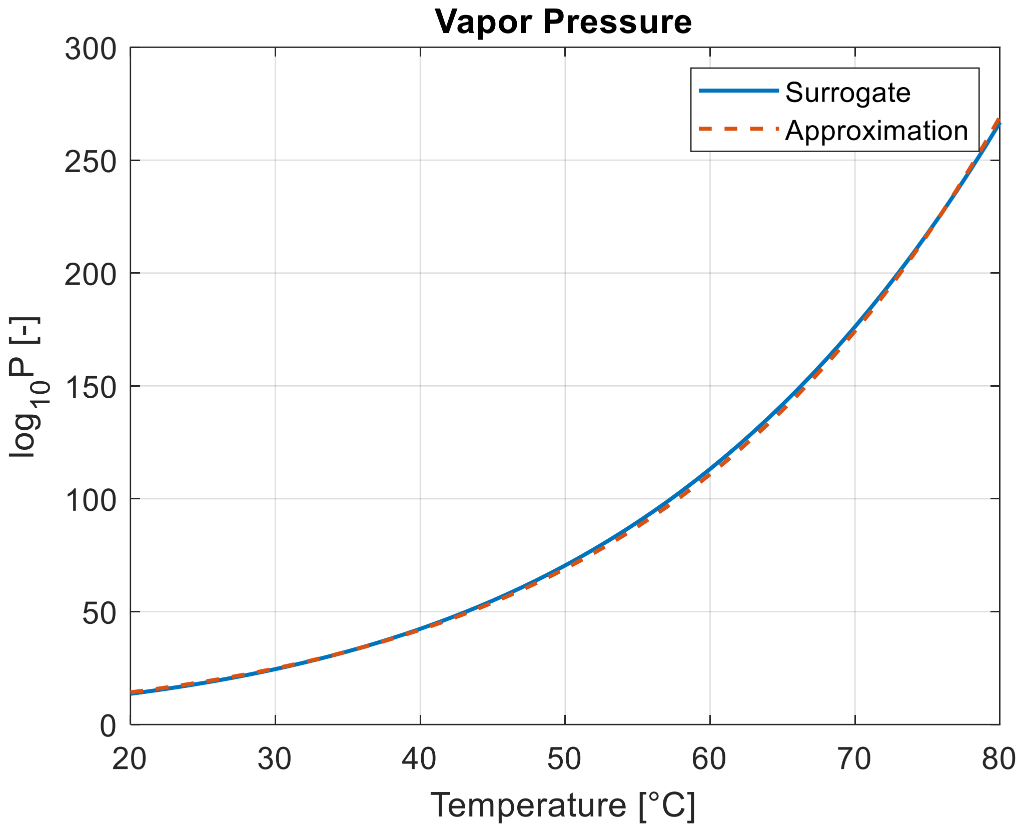

Figure 31 *Vapour pressure comparison.*

About the enthalpy of vaporisation, the regression equation for the is:

$$\Delta H_{vap} = A\left(1 - \frac{T}{T_c}\right)^n \tag{51}$$

Where ΔH_{vap} is the enthalpy of vaporisation [J/kg] and A, T_c, n are the regression coefficients. In the is specified also the range of validity.

	Compound	A	T_c [K]	n	T_{min} [K]	T_{max} [K]
1	Levoglucosan	137.68	791.00	0.3637	455.40	658.00
2	Water	52.10	647.13	0.321	273.16	647.13
3	Vanillin	101.28	777.00	0.3860	355.00	777.00
4	Alkali Lignin	[-]	[-]	[-]	[-]	[-]
5	Ethylene Glycol	88.20	645.00	0.3970	260.15	645.00
6	Glycol Aldehyde	84.27	586.22	0.3827	370.20	404.5 0
7	2,5 Dimethylfuran	48.32	557.13	0.3800	177.34	557.13
8	Acetic Acid	35.14	591.95	0.3800	289.81	391.05
9	Oleic acid	109.02	781.00	0.3940	286.53	781.00

Table 14 *Regression coefficients for the evaluation of enthalpy of vaporisation.*

The enthalpy of vaporisation of the mixture can be approximated as:

$$\Delta H_{vap_m} = \sum_i x_i \Delta H_{vap_i} \tag{52}$$

Where x_i is the mole fraction of the *i*-th species and ΔH_{vap_i} is the enthalpy of vaporisation of the *i*-th pure species.

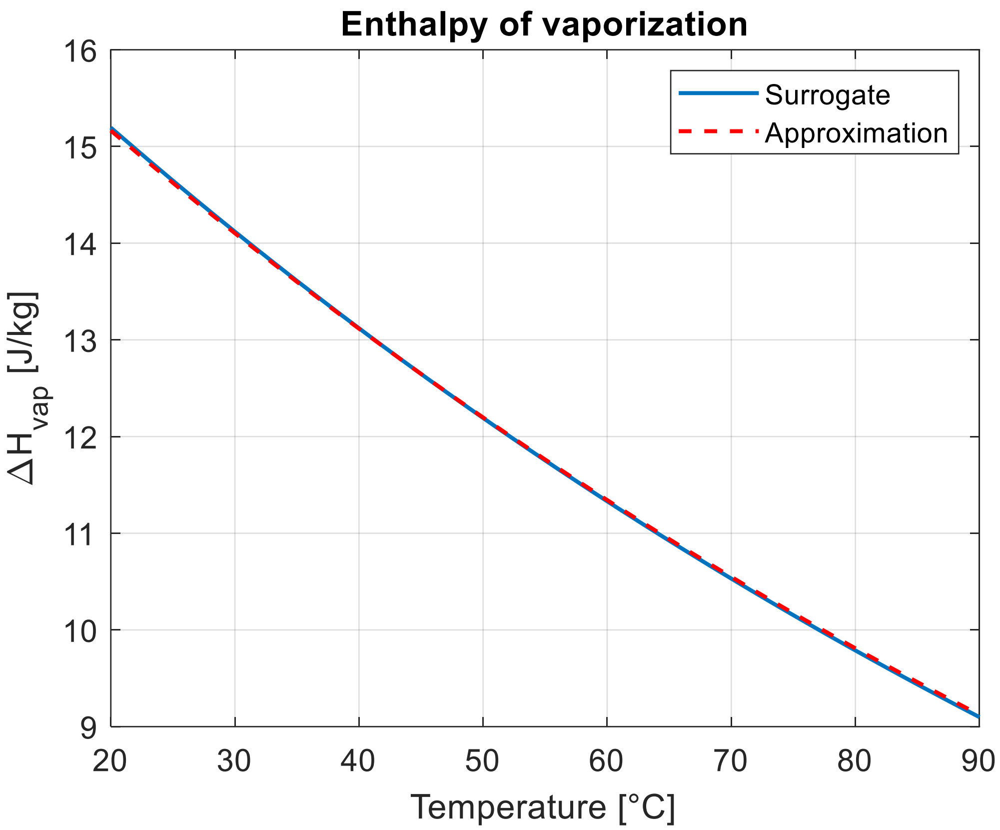

Figure 32 *Enthalpy of vaporization comparison.*

In literature, it has not been found data suitable with the sample Ext-A about the vapour pressure and enthalpy of vaporization. So, these two properties could not have been validated by comparison with experimental data.

9. Model Creation

The final purpose of this thesis was to create a CFD model that could simulate the experimental work chosen and summarized in the chapter 7.

This part was completed in the following way:

1. Creation of the 3D model,
2. Imposition of the boundaries,
3. Implementation of the case setup,
4. Simulation of the 3D model,
5. Post-processing of the results.

As already said, the VOF-Spray One-Way Coupling includes two different simulations, therefore the steps above listed have been repeated twice.

9.1 3D Model – VOF simulation

The nozzle used in the test is the air blast atomizer P/N 30609 supplied by Delavan. About the internal geometry of this model there are not many data, so that some assumptions were needed.

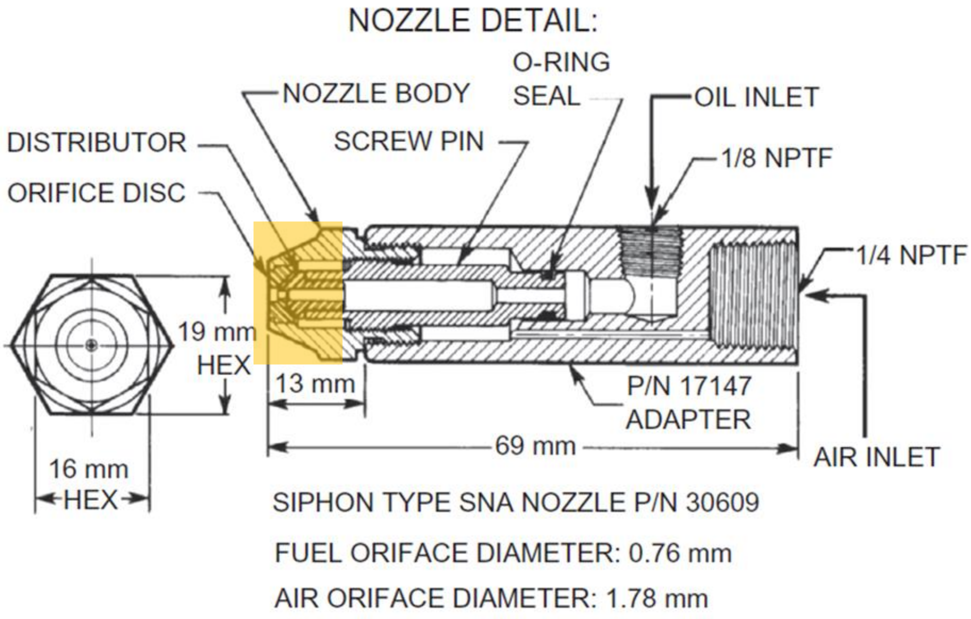

Figure 33 *Schematic of the air-blast atomizer P/N 30609.*

In the catalogue supplied by Delevan [13] it is present a sketch of the 2D section of the nozzle (see **Figure 33**). From this scheme it is shown that there are two inlets, one for the fuel and a second for the air.

Moreover, the nozzle can be moved up and down, regulating in this way the air flow rate that is mixed with the fuel mass flow. More details can be seen in the **Figure 34**, particularly, it is possible to notice that the air channel is sloped of around 45° with respect to the fuel one.

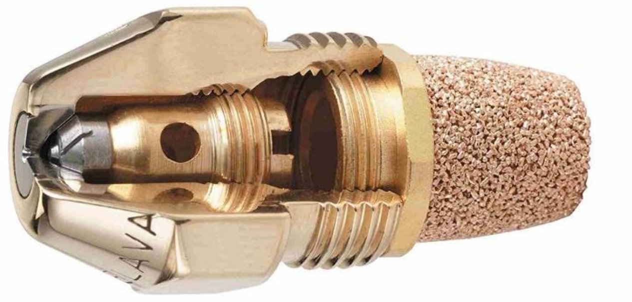

Figure 34 *Section of the air-blast atomizer P/N 30609.*

Jonathan A. Martin and Akwasi A. Boateng, in their study on the combustion performance of FPBO blended with ethanol, used the same air blast atomizer P/N 30609 supplied by Delevan [14]. And in particular, they reported the measure of the outlet fuel orifice diameter ($D_o = 0.76\ mm$), which was fundamental to schematize the 3D sketch of the nozzle.

As first assumption has been decided to simulate only the section highlighted in the yellow box of the Figure 33. An initial version of the 3D model has been made with the software SOLIDWORKS, then the CAD file has been converted into STL file, to be correctly imported in CONVERGE. Once the model was imported on CONVERGE it has been modified directly there.

The control volume is characterized by a central fuel channel with around an annular channel for the atomizing air. The air channel converges towards the mixing chamber with and inclination of 45°. In the mixing chamber, the air flow meets the fuel flow, resulting in a first atomization (see Figure 35). After that, the mixed flow exits from the nozzle passing through the outlet orifice (whose diameter has been assumed to be $0.64\ mm$), and so a second atomization takes place. The space outside the nozzle is represented by an outlet chamber, which shape can be arbitrarily chosen considering computational reasons.

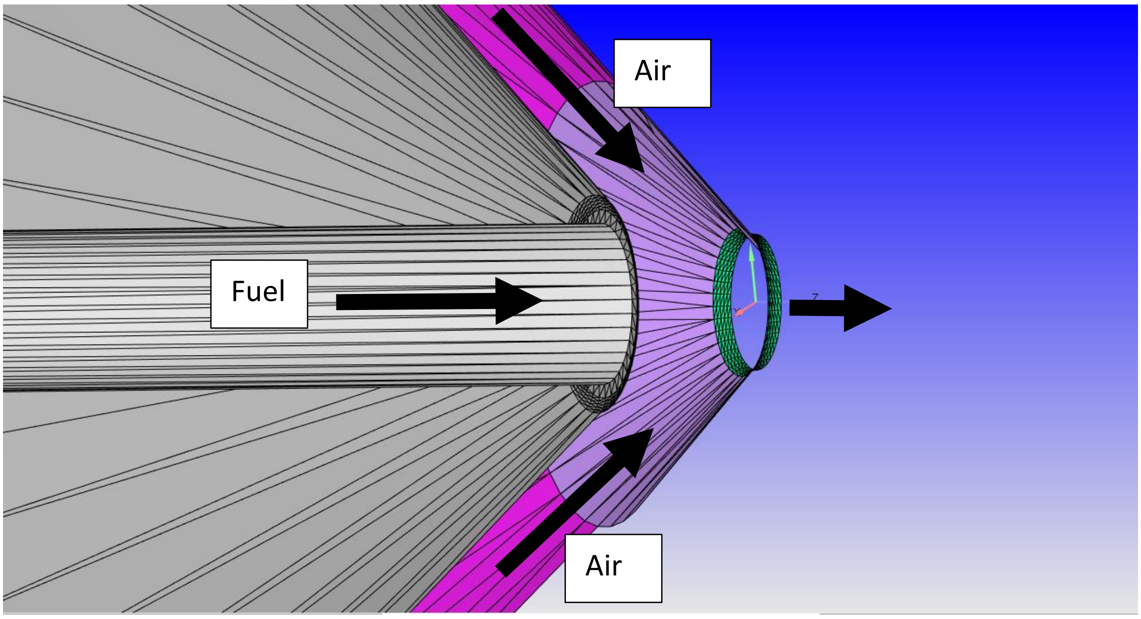

Figure 35 *Nozzle 3D Model detail – Mixing chamber*

The last version of the 3D model is shown in the **Figure 36**. The differences with respect to the initial version are the fuel and air channels longer, giving more space to the flows to better develop, the initial parts of both the channels have a larger cross section that gradually decreases until the assumed diameter is reached. Finally, the outlet chamber (the light blue sphere in the picture) has been modified from a cylindrical shape to a spheric one, because, as already said previously, in the VOF simulation, only the data of the two layers by the outlet orifice are necessary for the following simulation. So, since in this phase what happen beyond these two layers is not relevant, the control volume can be reduced in favour of the computational time.

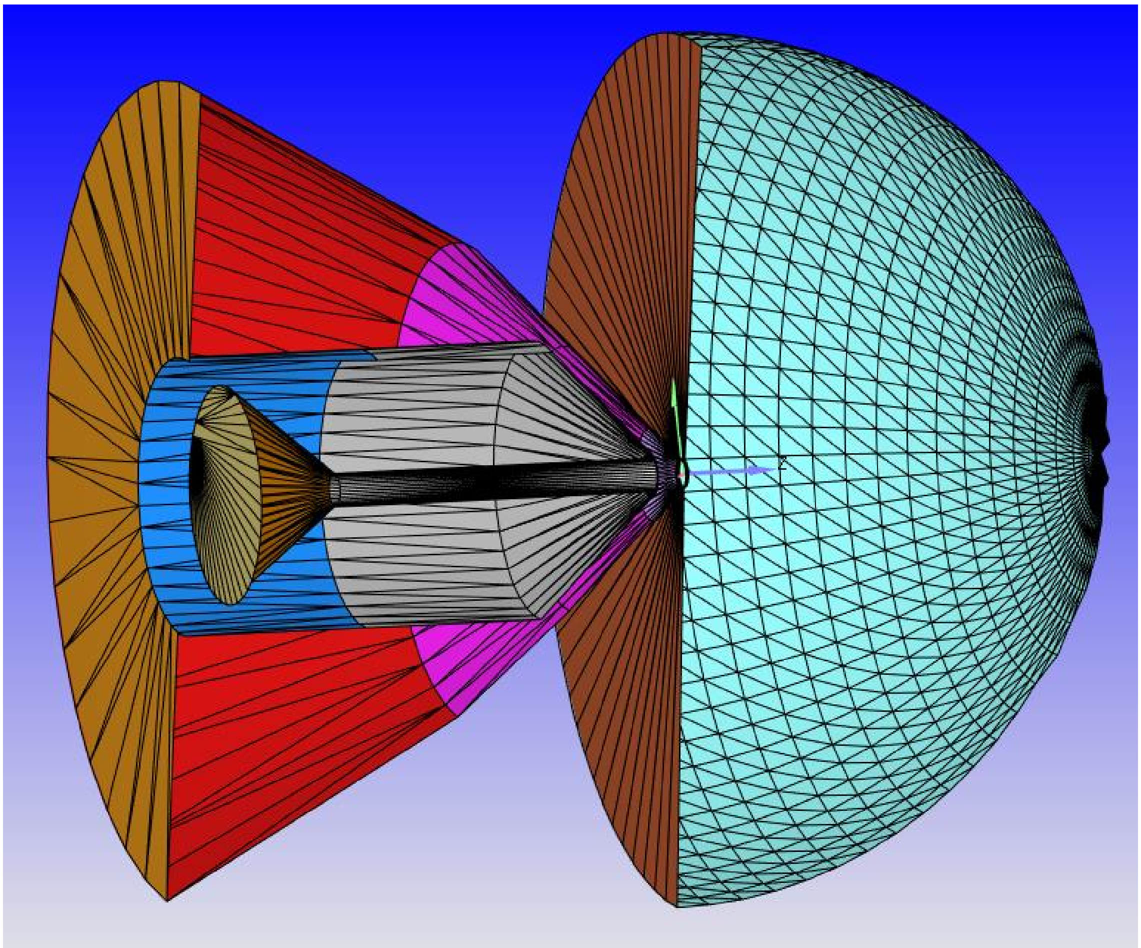

Figure 36 *3D model*

9.2 Boundary Conditions and Case Setup – VOF simulation

When the geometry is done, it is needed to define the boundaries, the regions and next the boundary conditions.

There are different types of boundaries on CONVERGE: inflow, outflow, wall, symmetry, periodic, two_d, gt-suite, and interface. At each boundary is associated a boundary condition which can be a Dirichlet (53) or Neumann type (54).

$$\phi = f \tag{53}$$

$$\frac{\partial \phi}{\partial x} = f \tag{54}$$

Where ϕ is a general solved quantity and f is the specified value or derivative on the boundary.

Generally, the most common boundary types used are outflow, inflow, and wall. The outflow and inflow are similar but not the same, in fact, for example in the outflow type it is necessary to set boundary conditions for backflow, which is the amount of flow entering from the outflow boundary. Moreover, bad setting of inflow and outflow boundaries can seriously affect the converge of the solution. Wall boundaries in CONVERGE can be moving or fixed.

Thanks to these boundaries, parameter such as velocity, pressure, temperature, turbulent kinetic energy, turbulent dissipation, and specific dissipation rate can be imposed on the entire surface associated to the boundary.

In this specific case, the boundaries are:

- Fuel_inlet: it is an inflow boundary. In this boundary has been imposed the fuel mass flow rate (0.76 kg/s) and the temperature (60°C).
- Air_inlet: it is an inflow boundary, in which has been imposed the air flow rate (15LPM) and the temperature (25°C).
- Chamber_outlet: it is an outflow boundary.
- Chamber_wall: it is a wall boundary, in this boundary has been imposed the temperature (25°C).
- First_breakup_chamber_wall: it is a wall boundary, in this boundary has been imposed the temperature (25°C).
- Fuel_wall: it is a wall boundary, in this boundary has been imposed the temperature (60°C).
- Air_inner_wall: it is a wall boundary, in this boundary has been imposed the temperature (25°C).
- Air_outer_wall: it is a wall boundary, in this boundary has been imposed the temperature (25°C).
- Orifice_wall: it is a wall boundary, in this boundary has been imposed the temperature (25°C).

- Fuel_tank_wall: it is a wall boundary, in this boundary has been imposed the temperature (60°C).

Note that both the inlet boundaries condition can be setup to change in time, and in this case the inlet mass flows are zero at the starting time and gradually increase until, after 0.0005s, they reached the regime values.

Each boundary needs to be associated to a Region, the way used by CONVERGE to initialize variables, such as temperature, pressure, velocity, turbulent kinetic energy, turbulent dissipation, species, and passives.

In this project have been defined four different regions:

- Fuel: it includes Fuel_wall boundary. In this region there is only FPBO at 60°C.
- Air: it includes Air_inlet, Air_inner_wall and Air_outer_wall. In this region there is only air at 25°C.
- First breakup chamber: it includes First_breakup_chamber_wall and Orifice_wall. In this region there is only air at 25°C.
- Chamber: it includes Chamber_outlet and Chamber_wall. In this region there is only air at 25°C.
- Fuel tank: it includes Fuel_tank_wall and Fuel_inlet. In this region there is only FPBO at 60°C.

Note that in all the regions the pressure is initialise at 1atm and the velocity at 0m/s. Therefore, all the domain is initialised with only air, except for the *fuel* and the *fuel tank* regions, which are already full of FPBO from the initial time (t=0s). Moreover, in the *regions and initialization* field, the FPBO fuel has been specified adding each component and the corresponding mass fraction. Because if a composite specie is insert, directly, as a single component the *vof_spray.out* will not be printed.

To complete the case setup, it is necessary to also fill the following sections: materials, simulations parameters, physical models, the grid control, out/post-processing.

9.2.1 Materials

FPBO is not already available on CONVERGE database, for this reason the selection of a surrogate was needed. More details about the characterization of the surrogate are in the chapter 8.

9.2.2 Simulation parameters

In this section it is possible to choose if performing a transient or a steady state simulation. In this specific case the simulation is a transient type. In fact, the simulation has an initial transitory, where boundary conditions are reaching the regime values, after that the simulation, theoretically, stabilizes to a steady state condition.

Other parameters that are imposed in this phase are the start (t=0s) and end (t=0.1s) time of the simulation, the computational time for each time step and the CFL limits, which are important for the stability of the simulation.

9.2.3 Physical Models

In the Physical Models section is it possible to select the turbulent models, in this specific case it has been choose the Standard k-ε RANS model. Then, for the first simulation has been selected the VOF model and for the second the Spray one.

Note that as VOF model has been chose the No Front Tracking one and the cavitation phenomena has been neglected.

9.2.4 Grid Control

For the mesh of this domain has been chose a base grid of 1mm, and then the more critical locations have been refined using the AMR and Fixed Embedding tools.

The AMR automatically activate where the sub-grid scalar field is smaller than 0.1m/s for the velocity and 0.001 for the void fraction.

The fixed embeddings are located in the area of the mixing chamber and at the outlet of the nozzle. In the walls of the fuel and air channel, the embeddings are activate because a wall treatment is necessary to solve the viscous sub-layer.

9.2.5 Out/Post-processing

The main scope of this section is to indicate which parameter values CONVERGE has to calculate each time step. All these values will be collected in the output files, which are usable by users to analyse the results.

In this specific case, the parameter values that have been considered interesting to print out are the void fraction, the temperature, the pressure, the density, and the velocity fields evolution.

9.3 3D Model – Lagrangian simulation

The Lagrangian simulation is simpler to prepare than the VOF one. The control volume can be assumed to be just a cylinder, since it represents the space outside the nozzle, where the fuel is sprayed. To be sure to correctly simulate the spray, the cylinder has to be large enough to include all the points that will be reached by the droplets of the spray.

In this case the cylinder has a diameter around 10 times larger than the orifice one and a length of 13cm (see **Figure 37**).

The cylinder is positioned in the space so that the orifice of the nozzle is within the control volume and not on some surface or worst outside.

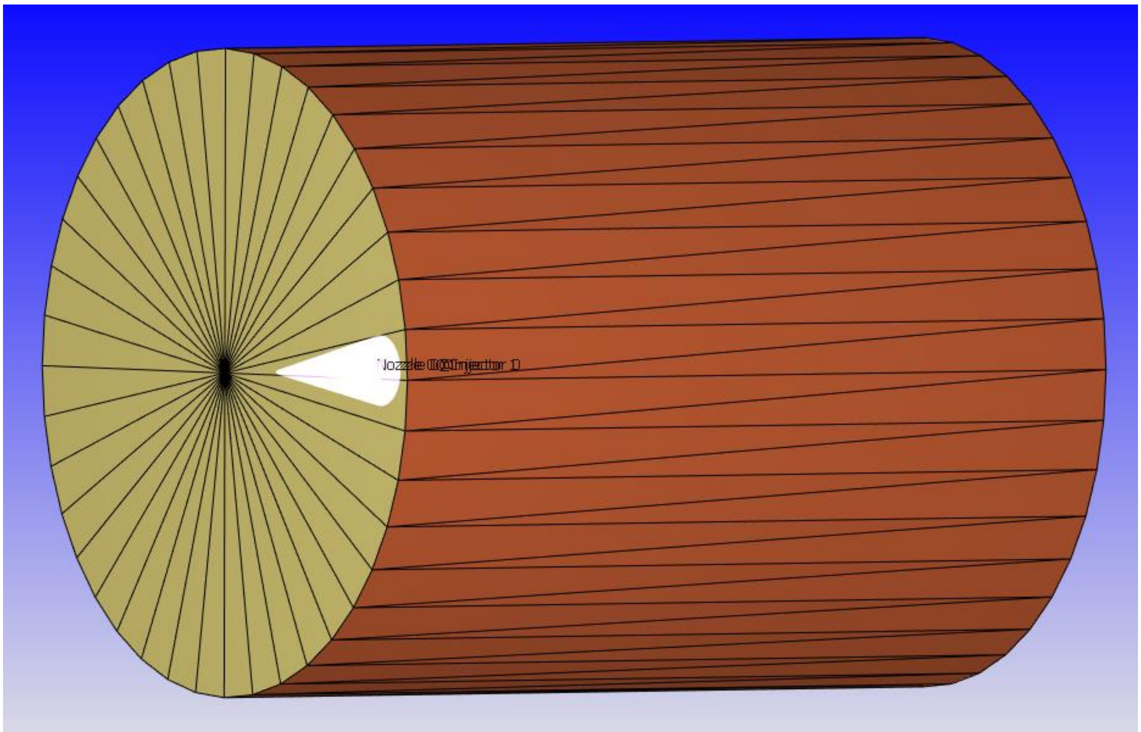

Figure 37 *The control volume of the Lagrangian simulation.*

9.4 Boundary Conditions and Case Setup – Lagrangian simulation

The boundaries associated to the surfaces of the control volume are called: Wall, Back and Front. All three are wall boundaries and the temperature is fixed at 25°C.

There is only one region, called *Chamber*, which is initialised with air at 25°C, pressure at 1atm and velocity at 0m/s. Obviously, all the boundaries are associated to the same and single region.

9.4.1 Materials

As already done in the VOF simulation, here the FPBO surrogate is used, but as *parcel* and not as a liquid. Usually, the *liquid simulation* is for configuring properties of a Eulerian liquid (such as for volume of fluid simulations) while *parcel simulation* is for configuring properties of Lagrangian liquid parcels (such as for spray simulations). Otherwise, these two dialog boxes operate in the same manner and contain the same fields and tools.

9.4.2 Simulation parameters

The simulation parameters are the same that have been chosen for the VOF part.

9.4.3 Physical Models

For this second simulation it has been selected the Standard k-ε RANS model for the turbulent model. Then the VOF model has been substituted by the spray model. Note that in the spray modelling, the evaporation phenomena has been assumed to be negligible for the lack of data.

After that, the injectors need to be specified, in this specific case there are two injectors, the first is the inlet of the mixing chamber and the second one is the outlet of the nozzle. The model used to characterize the injectors is the KH+RT one, more details about this model are in the chapter 6.

9.4.4 Grid Control

The base grid in this second simulation is coarser than the VOF one, in fact the base grid is of 5mm. Anyway, the mesh close to the orifice outlet is finer (0.65mm), thanks to an embedding with a conical shape.

The AMR automatically activate where the sub-grid scalar field is smaller than 0.1m/s for the velocity.

9.4.5 Out/Post-processing

In this spray simulation it has been considered useful to print out the output files of the temperature, pressure, density, and velocity fields evolution, and about the parcel the radius, the velocity, the temperature, and the number of drops.

10. **Results**

In this chapter the results are discussed and when possible validated with experimental data.

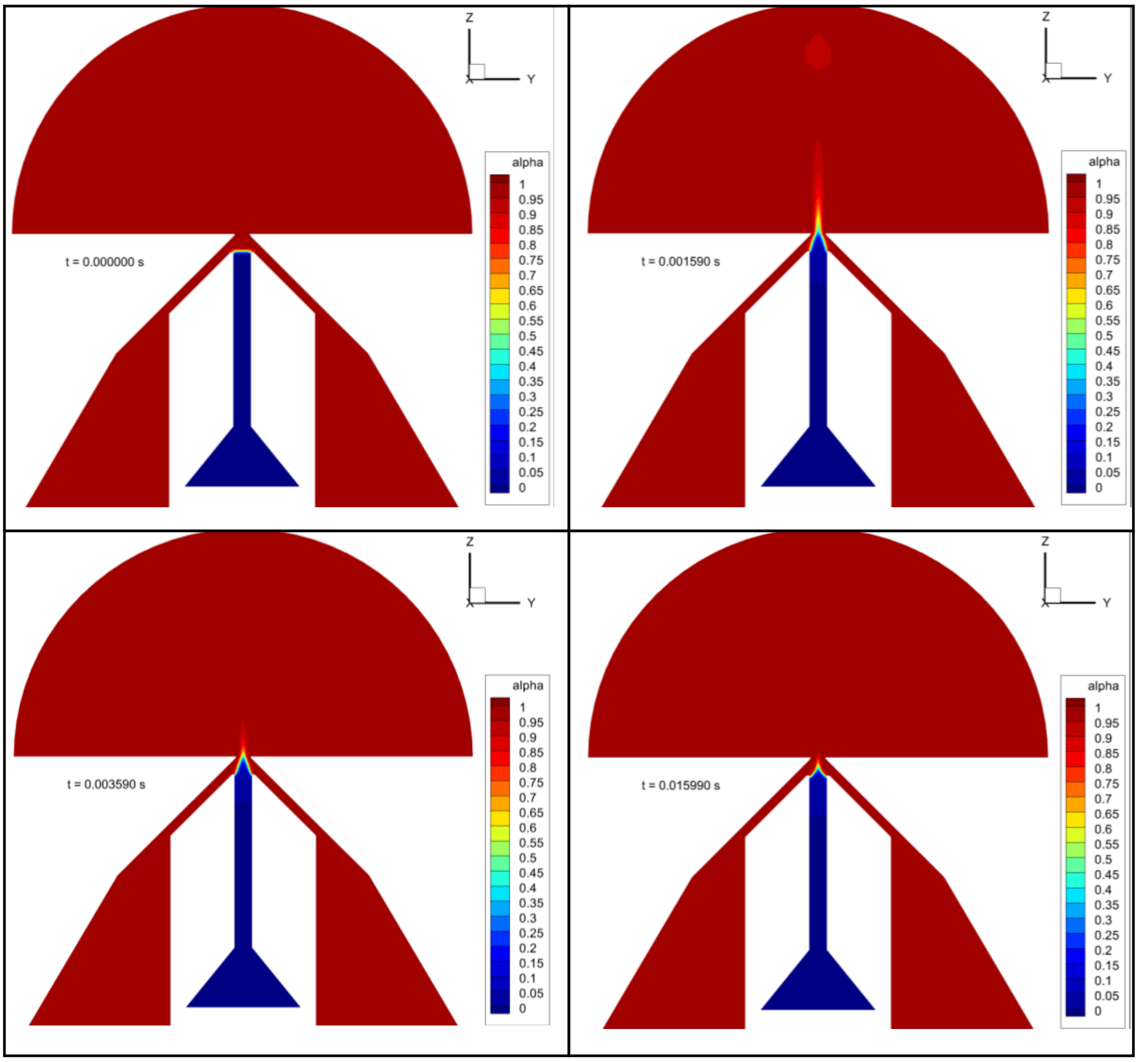

Figure 38 *Alpha distribution.*

In the **Figure 38** are shown the cross sections, along the z-y plane, of four fames. The variable called *alpha* represents the void fraction, the red areas correspond to alpha equal to 1, and so in the cells only gas is present. On the opposite side, the blue areas correspond to alpha equal to zero and so only liquid is in the cell, the other colours are referred to intermediate values.

At the initial instant, anything is moving, but immediately after FPBO and air start to come out. As results of that, a sort of liquid tail is generated, and after some instants a sphere of fuel broke off. The liquid tail becomes even smaller until the boundary conditions reach the regime values. Around 0.009s the liquid tail stops to vary its shape and alpha distribution continues to be the same until the end of the simulation (see **Figure 38** - frame right-bottom). This alpha distribution is coherent with the example SPRAY-G.

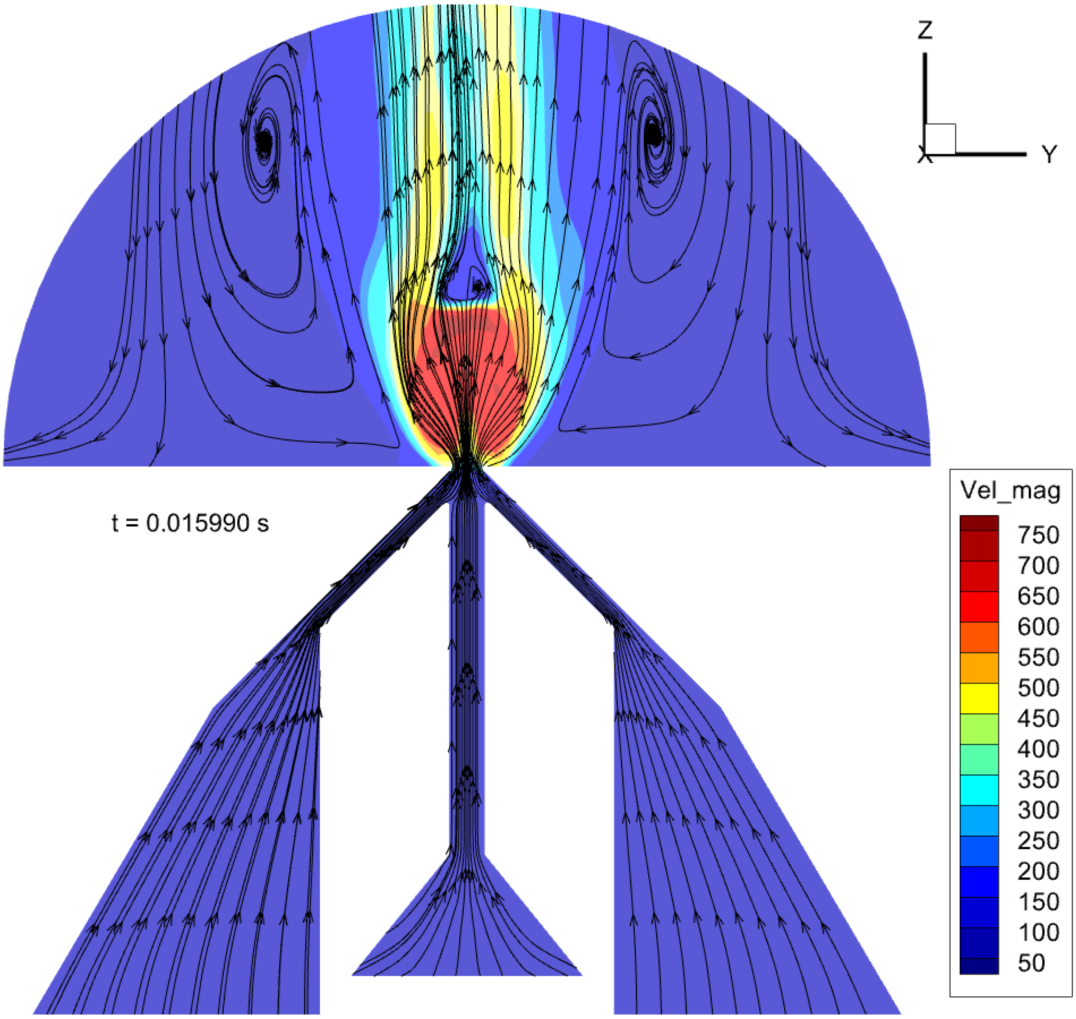

Figure 39 *Velocity field and streamlines.*

In the **Figure 39** is shown the velocity field and as expected the velocity is higher at the exit of the nozzle and lower far from it. Due to the lack of data, it is not possible to verify if the velocities values correspond to the reality.

For a better analysis, in **Figure 40** are shown the velocity field in the fuel channel and a detail of the mixing chamber. As expected, the velocity of the fuel is smaller close to the wall and higher in the middle. Moreover, the velocity at the exit of the air channel is lower of 100m/s and this is coherent with the characteristics of air-blast nozzles.

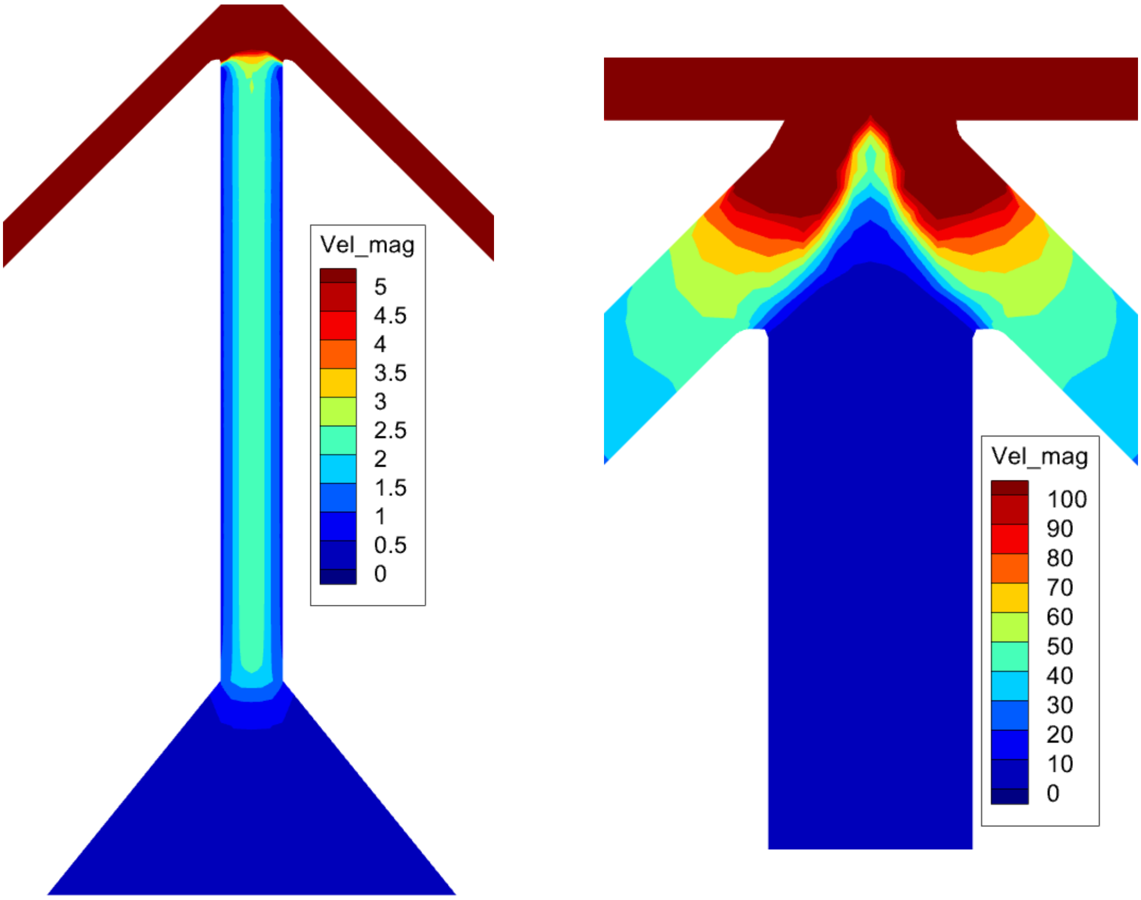

Figure 40 *Detail of velocity field in the fuel channel and mixing chamber.*

Once the VOF simulation was completed, the Lagrangian one was performed, and the results are here shown below. The main result is the 3D reproduction of the spray (see **Figure 41)**.

The radius of the droplets varies in a range between 50 microns and 450 microns. As expected, the larger droplets are near the exit of the nozzle. Note that, in the numerical reproduction all the droplets have a spheric shape, even if in the reality they should have an irregular shape. Moreover, also the ligaments are represented by spheres, but as know, they have a more elongated shape.

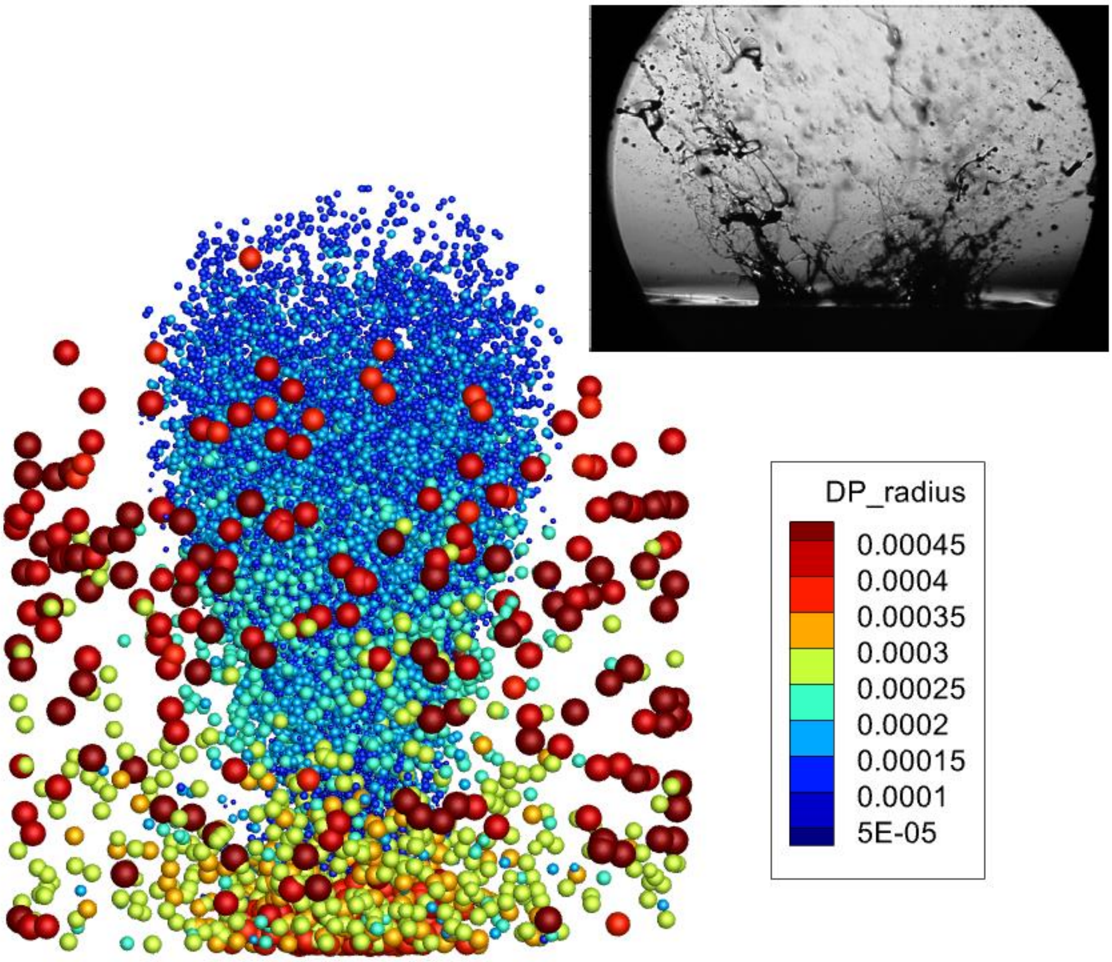

Figure 41 *Comparison: spray obtained by numerical simulation vs experimental one.*

Another aspect that can be compared is the penetration length, which is around 10 cm in both sprays.

So, after all, it can be noticed a good similarity between the numerical spray and the experimental one.

The last parameter to validate, and the most relevant, is the SMD (see **Figure 42**).

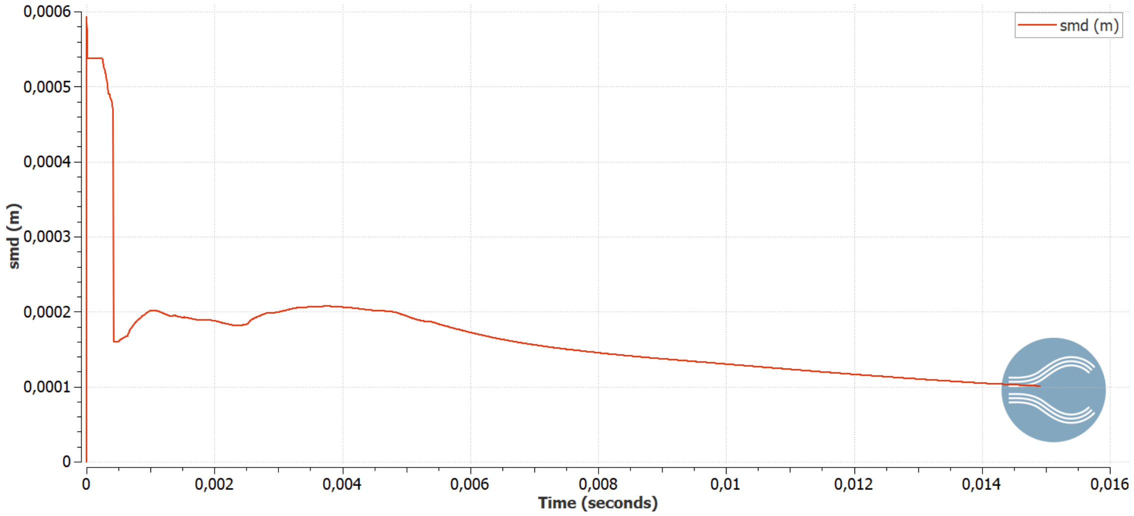

Figure 42 *SMD of the numerical spray.*

In the graph is shown the evolution of the SMD from the beginning to the end of the simulation. The SMD, has high values in the initial part of the transitory, when the boundary conditions are not yet constant. Anyway, passed this phase, the SMD decreases to a value around 100microns.

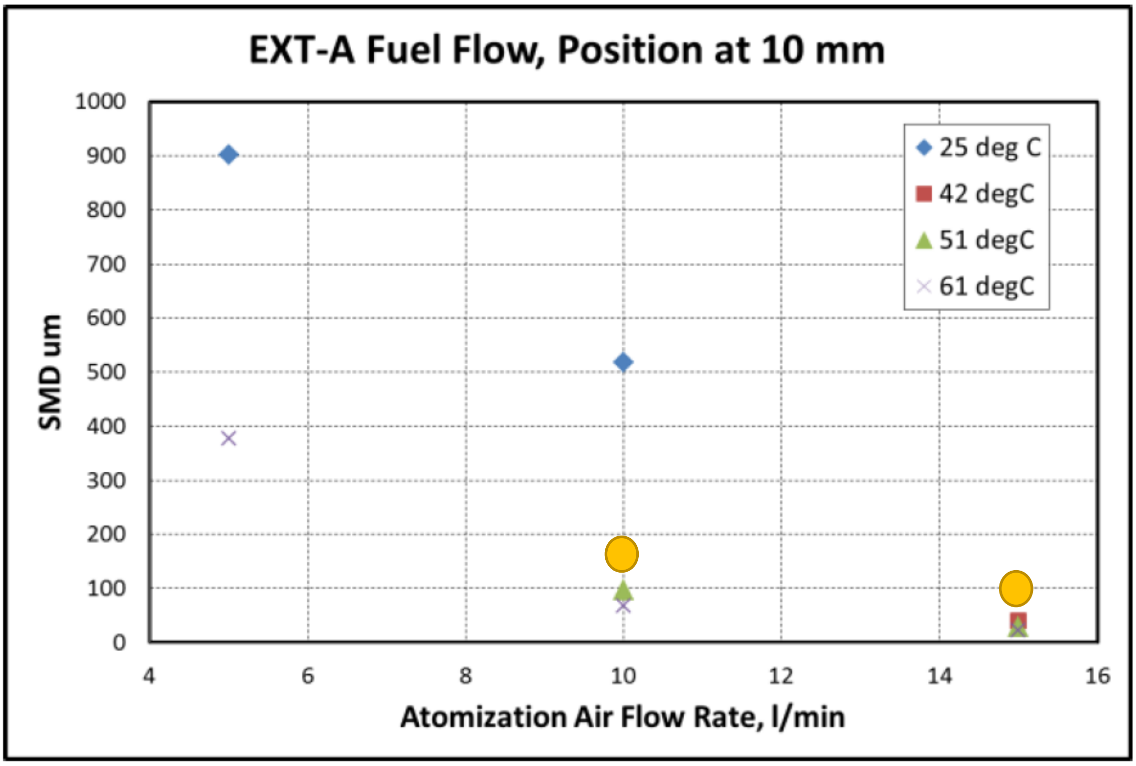

Figure 43 *Comparison between the numerical SMD and the experimental one.*

A second test have been performed, with an air flow rate of 10 LPM and the fuel at 60°C, obtaining a SMD of about 150microns.

By a comparison between the numerical SMD and the experimental one (see **Figure 43**), the numerical SMD (the yellow dot in the figure) is about twice higher the experimental one. Anyway, these results can be considered acceptable since the several approximations that have been done in the geometry, in the fluid characterization and in the numerical model.

11. **Conclusion**

In this thesis it has been developed a numerical model to simulate the atomization of FPBO. This was a challenging task due to the lack of data about the FPBO and its atomization in literature. In fact, FPBO and its applications are yet object of study from many researchers.

To develop this numerical model was necessary the selection of a reference experimental work. With a view of future application of FPBO in gas turbines, a selection parameter was the achievement of SMD about 50microns. Moreover, as widely demonstrated in literature, a good atomization of this specific oil is possible only using a twin fluid atomizer, and even better if it is an internal mixing one. For this project the test selected was performed by S.Yun and his colleagues. S.Yun and his colleagues obtained an SMD of 50microns, using an air blast nozzle, 15LPM of atomizing air and 0.73g/s of FPBO heated up to 60°C.

Once the reference model was selected, the characterization of a surrogate for FPBO was required. As already known, the physical and chemical properties of FPBO are strongly dependent on the type of feedstock. For this reason the surrogate proposed by A.Frassoldati and his colleagues has been used as starting point, but then it was adapted to the physical properties of the FPBO sample used by S.Yun in his experimental work. It was necessary to refine properties such as viscosity, density and surface tension, due to the notable difference between the surrogate of A.Frassoldati and the values reported by S.Yun.

In the following step, the 3D model of the nozzle was defined. But, in this phase many approximations about the geometry were needed. Only the orifice diameter of the fuel channel and the inclination of air channel were known. Nevertheless, an error around $\pm$ 0.5mm is estimated for the other measurements, such as the outlet diameter of the nozzle. Once the geometry was ready, it was imported on CONVERGE, where other small modifications have been done and the mesh was defined. In particular, the tools AMR and fixed embedding have been used, in order to have a base grid coarse and a finer one only where necessary, in favour of the computational time.

On CONVERGE was setup the numerical model. To be more precise, the model called *VOF-Spray One-Way Coupling* was used. The advantage to use this method was to combine a high-fidelity simulation of a fuel injector and nozzle (VOF) with a low-cost parcel-based fuel injector spray simulation (Lagrangian).

Generally, to perform both simulation (VOF and Lagrangian one), 4 days were required. The number of cells was around 200000 for the VOF and 10000 for the Lagrangian one.

The result is a comparable reproduction of the experimental work of S.Yun, in fact the numerical spray has a similar shape compered to the original one and the SMD obtain is around 100 microns, which is a good results taking into account all the approximations done.

11.1 Future directions

The numerical model achieved acceptable results, but in future it could be improved more. For example, thanks to the geometrical symmetry, the control volume can be reduced (using the Periodic Boundaries) and so obtaining a considerably reduction of the computational time.

Another weak point, that can be improved regards the characterization of the surrogate. A better characterization is required to consider more phenomena of atomization, such as the cavitation. Therefore, the chemical properties, which have been treated marginally in this thesis, because the lack of data, but which is fundamental if this oil will be applied in combustion models.

Finally, the geometry and setup of the model can be better calibrated, to perform better results.

Bibliography

[1] A. Sharma, *Introduction to Computational Fluid Dynamics*, vol. M. 2016.

[2] A. H. Lefebvre and V. G. Mcdonell, *Atomization and Sprays, Second Edition.* 2017.

[3] J. O. Hinze, *Fundamentals of the hydrodynamic mechanism of splitting in dispersion processes*. 1955.

[4] A. H. Lefebvre and V. G. McDonell, *Atomization and sprays*. 2017.

[5] M. Broumand, S. Albert-Green, S. Yun, Z. Hong, and M. J. Thomson, “Spray combustion of fast pyrolysis bio-oils: Applications, challenges, and potential solutions,” *Prog. Energy Combust. Sci.*, vol. 79, p. 100834, 2020, doi: 10.1016/j.pecs.2020.100834.

[6] J. Lehto, A. Oasmaa, Y. Solantausta, M. Kytö, and D. Chiaramonti, “Fuel oil quality and combustion of fast pyrolysis bio-oils,” *VTT Publ.*, no. 87, p. 79, 2013, doi: http://dx.doi.org/10.1016/j.apenergy.2013.11.040.

[7] J. Lehto, A. Oasmaa, Y. Solantausta, M. Kytö, and D. Chiaramonti, “Review of fuel oil quality and combustion of fast pyrolysis bio-oils from lignocellulosic biomass,” *Appl. Energy*, vol. 116, pp. 178–190, 2014, doi: 10.1016/j.apenergy.2013.11.040.

[8] P. Roy and G. Dias, “Prospects for pyrolysis technologies in the bioenergy sector: A review,” *Renew. Sustain. Energy Rev.*, vol. 77, no. May 2016, pp. 59–69, 2017, doi: 10.1016/j.rser.2017.03.136.

[9] M. Buffi, A. Cappelletti, A. M. Rizzo, F. Martelli, and D. Chiaramonti, “Combustion of fast pyrolysis bio-oil and blends in a micro gas turbine,” *Biomass and Bioenergy*, vol. 115, no. April, pp. 174–185, 2018, doi: 10.1016/j.biombioe.2018.04.020.

[10] K. D. Redfern and K. Redfern, “Utilization of pyrolysis oil in industrial scale boilers by,” 2013.

[11] M. Broumand, M. Shahzeb Khan, S. Yun, Z. Hong, and M. J. Thomson, “The role of atomization in the spray combustion of a fast pyrolysis bio-oil,” *Fuel*, vol. 276, no. March, p. 118035, 2020, doi: 10.1016/j.fuel.2020.118035.

[12] S. Yun, M. Choi, and A. Kumar, “Evaluation of spray performance of pyrolysis oil,” *Proc. ASME Turbo Expo*, vol. 3, pp. 1–9, 2019, doi: 10.1115/GT2019-91742.

[13] D. Inc., “Oil Burner Nozzles and Accessories - for residential applications,” 2000, [Online]. Available: http://www.delavaninc.com/pdf/catalog.pdf.

[14] J. A. Martin and A. A. Boateng, “Combustion performance of pyrolysis oil/ethanol blends in a residential-scale oil-fired boiler,” *Fuel*, vol. 133, pp. 34–

44, 2014, doi: 10.1016/j.fuel.2014.05.005.

[15] M. Pelucchi, C. Cavallotti, A. Cuoci, T. Faravelli, A. Frassoldati, and E. Ranzi, “Detailed kinetics of substituted phenolic species in pyrolysis bio-oils,” *React. Chem. Eng.*, vol. 4, no. 3, pp. 490–506, 2019, doi: 10.1039/c8re00198g.

[16] A. Stagni, T. Faravelli, R. Calabria, and P. Massoli, “Project title:,” no. 654650, pp. 1–40, 2020.

[17] Carl L. Yaws, *Thermophysical Properties of Chemicals and Hydrocarbons*. 2015.

[18] B. E. Poling and J. M. Prausnitz, *THE PROPERTIES OF GASES AND LIQUIDS*. .

[19] A. Oasmaa, T. Ohra-aho, and C. Lindfors, “Physico-chemical properties of FPBO,” no. 654650, pp. 1–24, 2020.

[20] D. Wissmiller, R. C. Brown, and T. R. Meyer, “Pyrolysis oil combustion characteristics and exhaust emissions in a swirl-stabilized flame,” vol. Doctor of, no. Paper 10889, p. 217, 2009.

[21] I. M. Rocha, T. L. P. Galvão, E. Sapei, M. D. M. C. Ribeiro Da Silva, and M. A. V. Ribeiro Da Silva, “Levoglucosan: A calorimetric, thermodynamic, spectroscopic, and computational investigation,” *J. Chem. Eng. Data*, vol. 58, no. 6, pp. 1813–1821, 2013, doi: 10.1021/je400207t.

[22] M. Petitjean *et al.*, “Vapor Pressure Measurements of Hydroxyacetaldehyde and Hydroxyacetone in the Temperature Range (273 to 356) K To cite this version : HAL Id : hal-02308893,” 2020.

List of Figure

Acknowledgement

Prima di tutto, vorrei ringraziare i miei relatori Mirko Baratta, Daniela Misul e Simone Salvadori per avermi concesso l'opportunità di lavorare con loro. Ma soprattutto, vorrei ringraziarli per il sostegno e la disponibilità mostratami in questi mesi, che mai ho dato per scontato. Un altro ringraziamento va anche al professore David Chiaramonti e al Dott. Ing. Marco Buffi, per il loro tempo e la loro disponibilità, che sono stati fondamentali per lo svolgimento di questo progetto. Un ulteriore, e doveroso ringraziamento, va ad Alessandro e Prashant, che si sono sempre mostrati disponibili e amichevoli, non potevo chiedere di meglio.

Questa tesi segna la fine di un percorso che è iniziato un bel po' di anni fa e in questi ringraziamenti non posso non citare i miei coinquilini Giuliana e Nicolas, grazie ai quali sono riuscita a sentirmi a casa anche a Torino. Ma soprattutto Giuliana, con la quale oltre ad avere condiviso una stanza per tutti questi anni, ho condiviso la maggior parte delle mie esperienze Torinesi e non, da quelle più belle, a quelle più brutte (aggiungerei anche quelle pericolose). Definirti una semplice amica sarebbe riduttivo!

Un altro importante ringraziamento va a Chiara M., compagna di studio e di progetti. Dimensionare i condotti dell'aria non sarebbe stata la stessa cosa senza di te! Grazie per avere reso le nostre giornate al poli meno lunghe e pesanti.

Ringrazio anche tutte le persone fantastiche che ho conosciuto in Erasmus, Pilar, Carlos, Rocio e tutti gli altri. Ma soprattutto ringrazio l'Equipo, con i quali ho condiviso uno degli anni più incredibili. Un grazie speciale va a Chiara V., un'amicizia nata per caso, ma non per questo meno importante. Grazie per essere sempre così positiva.

Un ringraziamento lo meritano anche Cristina e Chiara L. Cristina che oltre ad essere una cugina e un'amica fantastica è anche il mio supporto informatico, grazie cri per tutta la pazienza che hai! E poi anche Chiara, che nonostante la distanza si è sempre rivelata un'ottima amica su cui contare, purché non si cammini molto!

Per concludere, un ultimo ringraziamento, e forse il più importante, va alla mia famiglia, la quale mi ha sempre supportata. Senza il loro aiuto nulla di tutto ciò sarebbe stato possibile. Grazie mamma e papà.